

Pharmacological Characterisation of Novel Adenosine Receptor A₃R Antagonists

Kerry Barkan¹, Panagiotis Lagarias², Eleni Vrontaki², Dimitrios Stamatis², Sam Hoare³, Karl-Norbert Klotz⁴, Antonios Kolocouris^{2*} and Graham Ladds^{1*}

Running Title: Novel antagonists of the A₃R.

¹ Department of Pharmacology, University of Cambridge, Tennis Court Road, Cambridge, CB2 1PD, UK.

² Section of Pharmaceutical Chemistry, Department of Pharmacy, School of Health Sciences, National and Kapodistrian University of Athens, Panepistimiopolis-Zografou, Athens, 15771, Greece.

³ Pharmechanics LLC, 14 Sunnyside Drive South, Owego, NY 13827, USA

⁴ Institute of Pharmacology and Toxicology, University of Würzburg, Versbacher Str. 9 97078 Würzburg, Germany

Address for correspondence:

Dr Graham Ladds, Department of Pharmacology, University of Cambridge, Tennis Court Road, Cambridge, CB2 1PD Tel; +44 (0) 1223 334020. Email: grl30@cam.ac.uk.

Dr Antonios Kolocouris, Department of Medicinal Chemistry, Faculty of Pharmacy, National and Kapodistrian University of Athens, Panepistimioupolis Zografou, Athens, 15 771. Tel: 210-727-4834, Email: ankol@pharm.uoa.gr.

Author Contributions:

KB, AK and GL conceived and designed the research; KB performed the mammalian assays; KK conducted radioligand binding experiments, PL, DS, EV and AK performed the molecular dynamic simulations; SH derived the equations for the 'Rapid competitor dissociation kinetics' model; KB, GL and AK analysed data; KB and GL wrote manuscript, AK revised and edited the manuscript.

Summary

Background and Purpose

The adenosine A₃ receptor (A₃R) belongs to a family of four adenosine receptor (AR) subtypes which all play distinct roles throughout the body. A₃R antagonists have been described as potential treatments for numerous diseases including asthma. Given the similarity between ARs orthosteric binding sites, obtaining highly selective receptor antagonists is a challenging but critical task.

Experimental approach

39 potential A₃R, antagonists were screened using agonist-induced inhibition of cAMP. Positive hits were assessed for AR subtype selectivity through cAMP accumulation assays. The antagonist affinity was determined using Schild analysis (pA₂ values) and fluorescent ligand binding. Further, a likely binding pose of the most potent antagonist (K18) was determined through molecular dynamics (MD) simulations and consistent calculated binding

free energy differences between K18 and congeners, using a homology model of A₃R, combined with mutagenesis studies.

Key Results

We demonstrate that K18, which contains a 3-(dichlorophenyl)-isoxazole group connected through carbonyloxycarboximidamide fragment with a 1,3-thiazole ring, is a specific A₃R (<1 μM) competitive antagonist. Structure-activity relationship investigations revealed that loss of the 3-(dichlorophenyl)-isoxazole group significantly attenuated K18 antagonistic potency. Mutagenic studies supported by MD simulations identified the residues important for binding in the A₃R orthosteric site. Finally, we introduce a model that enables estimates of the equilibrium binding affinity for rapidly disassociating compounds from real-time fluorescent ligand-binding studies.

Conclusions and Implications

These results demonstrate the pharmacological characterisation of a selective competitive A₃R antagonist and the description of its orthosteric binding mode.

Word count: 241

Keywords:

Adenosine A₃ receptor, antagonist, GPCR, mutagenesis studies, functional assay, cAMP, molecular dynamics, competitive antagonist, Schild analysis

Conflict of Interest

None for any author

Abbreviations

AR, adenosine receptor; A₁R, A₁ adenosine receptor; A_{2A}R, A_{2A} adenosine receptor; A_{2B}R, A_{2B} adenosine receptor; A₃R, A₃ adenosine receptor; CA200645, fluorescent xanthine amine congener; cAMP, adenosine 3',5' cyclic monophosphate; CHO, Chinese hamster ovary, DMSO, dimethyl sulfoxide; DPCPX, 8-cyclopentyl-1,3-dipropylxanthine; ERK, extracellular signal-regulated kinase; IB-MECA (1-deoxy-1-[6-[[[(3-iodophenyl)methyl]amino]-9H-purin-9-yl]-N-methyl-β-D-ribofuranuronamide), HEMADO, 2-hexyn-1-yl-N⁶-methyladenosine (HEMADO); MRS 1220, N-[9-chloro-2-(furan-2-yl)-[1,2,4]triazolo[1,5-c]quinazolin-5-yl]-2-phenylacetamide; NECA (5'-(N-ethylcarboxamido)adenosine); Nluc, Nano-luciferase; Nluc-A₃R, Nanoluc-labelled A₃ adenosine receptor; PMA (Phorbol 12-myristate 13-acetate); MD; molecular dynamic; MM-PBSA; Molecular Mechanics-Poisson Boltzmann Surface Area

INTRODUCTION

The adenosine A₃ receptor (A₃R), belongs to a family of four adenosine receptor (AR) subtypes (A₁R, A_{2A}R, A_{2B}R and A₃R), and is involved in a range of pathologies including cardiovascular, neurological and tumour-related diseases. In particular, mast cell regulation and myocardial preconditioning are key physiological processes regulated by the A₃R (Fredholm *et al.*, 2011). Unsurprisingly therefore, A₃R is a pharmaceutical target. Interestingly, the A₃R has been described as enigmatic, whereby many of the effects attributed to A₃Rs are contradictory (Gessi *et al.*, 2008). Despite this, A₃R antagonists having been described as potential treatments of asthma, chronic obstructive pulmonary disease (COPD) and glaucoma (Miwatashi *et al.*, 2008, Okamura *et al.*, 2004, Haeusler *et al.*, 2015), to name a few, and continuous research into both agonists and antagonists at the A₃R are warranted. One of the challenges associated with the druggability of the AR family has been the targeting of individual subtypes with sufficient specificity to limit off-target side effects (Chen *et al.*, 2013). *In silico* screening of vast compound libraries against receptor structures, known as structural-based drug design, offers huge potential in the development of highly selective ligands.

Although all AR members are activated by the endogenous agonist adenosine, the A_{2A}R and A_{2B}R are predominantly G_s-coupled whereas A₁R and A₃R generally couple to G_{i/o}. This classical pathway following A₃R activation and G_{i/o} coupling is the inhibition of adenylate cyclase (AC) resulting in a decrease in cAMP levels. Extracellular signal-regulated kinase 1/2 (ERK1/2) activation has also been described as downstream of A₃R and is reported to be dependent on βγ-subunits released from pertussis toxin (PTX)-sensitive G_{i/o} proteins, phosphatidylinositol-3-kinase (PI3K), the small GTP binding protein Ras, and MAP/ERK kinase (MEK) (Schulte and Fredholm, 2002). In addition to G_{i/o}, A₃R has also been reported to couple to G_q, leading to phospholipase C (PLC) activation and ultimately elevation of intracellular inositol 1,4,5-trisphosphate (IP₃) and calcium (Ca²⁺) levels (Gessi *et al.*, 2008).

The A_{2A}R is one of the best structurally characterised G protein-coupled receptors (GPCRs), with multiple crystal structures (both active and inactive) available including that bound to an engineered G protein (Carpenter *et al.*, 2016) and the A_{2A}R bound to the agonists (5'-(N-ethylcarboxamido)adenosine) (NECA) and adenosine (Lebon *et al.*, 2011), CGS 21689 (Lebon *et al.*, 2015), UK-432097 (Xu *et al.*, 2011) and the antagonists ZM241385 (Liu *et al.*, 2012, Doré *et al.*, 2011, Jaakola *et al.*, 2008), PSB36, caffeine and theophylline (Cheng *et al.*, 2017). Although the remaining AR subtypes have proven more difficult to crystallise with the A₃R structure yet to be resolved, there are a number of A₁R structures published including the adenosine-bound A₁R-G_i complex (Draper-Joyce *et al.*, 2018) and antagonist bound structures; DU172 (Glukhova *et al.*, 2017) and PSB36 (Cheng *et al.*, 2017). Thus, structural-based drug design offers huge potential in the development of highly selective ligands (Carlsson *et al.*, 2010, Katritch *et al.*, 2010, Lenselink *et al.*, 2016, Lagarias *et al.*, 2018). The limited availability of diverse high-resolution structures of the remaining AR subtypes bound to pharmacologically distinct ligands has meant there is a discrepancy between the capability to predict compound binding versus pharmacological behaviour; partial agonism, inverse agonism, biased agonist, antagonism, allosteric modulation etc (Sexton and Christopoulos, 2018). With this in mind, the potential antagonists (K1-K25, K28 and K35) identified in our previously published virtual screening investigation and binding experiments (Lagarias *et al.*, 2018) and some newly identified potential antagonists (K26, K27, K29-K34 and K36-K39)

were pharmacologically characterised using cAMP accumulation and ERK1/2 phosphorylation assays. We were able to identify a potent and selective A₃R antagonist, K18 (O4-[[3-(2,6-dichlorophenyl)-5-methylisoxazol-4-yl]carbonyl]-2-methyl-1,3-thiazole-4-carboximidamide) and, using molecular dynamic (MD) simulations combined with site-directed mutagenesis, elude to the potential binding site. Binding free energy calculations of similar in structure analogs of K18 were consistent with the proposed A₃R orthosteric binding area. Kinetic binding experiments of K5, K17 and K18 using a bioluminescence resonance energy transfer (BRET) method combined with functional assays led to the identification of important structural features of K18 for binding and activity. Further evaluation of this compound (and structurally related analogues) may afford a novel therapeutic benefit in pathologies such as inflammation and asthma.

RESULTS

Identification of A₃R selective antagonists

We set out to conduct a functional screen of 39 compounds for the identification of A₃R antagonists, some of which have previously been identified to bind one of the three AR subtypes; A₁R, A₃R or A_{2A}R (Lagarias *et al.*, 2018). Our screen was conducted using A₃R expressing Flp-In™-Chinese hamster ovary (CHO) cells where cAMP accumulation was detected following a combined stimulation of 1 μM forskolin (to allow A₃R mediated G_{i/o} response to be observed), 1 μM tested compound and the predetermined IC₈₀ concentration of NECA (3.16 nM). This initial screen was blinded with each compound numbered without the corresponding name or chemical structure (K1-39). Compound K1-39 were identified by unblinding (Table 1 and Supplementary Table 1) but are hereinafter referred to as their denoted 'K' number. For the purpose of structure-activity relationships studies, the new compounds (K26, K27, K29-K34 and K36-K39), were tested through this functional assay and radioligand binding (Supplementary Table 1). As expected, co-stimulation with 10 μM of both forskolin and NECA reduced the cAMP accumulation when compared to 10 μM forskolin alone and this was reversed with the known A₃R antagonist MRS 1220 (Table 1 and Supplementary Fig 1). Compounds K1, K10, K11, K17, K18, K20, K23, K25 and K32 were identified as potential antagonists at the A₃R through their ability to elevate cAMP accumulation when compared to forskolin and NECA co-stimulation. Of the nine potential A₃R antagonists, eight (K1, K10, K17, K18, K20, K23, K25 and K32) were confirmed as antagonists at the tested concentration of 1 μM (Supplementary Fig. 2 and Supplementary Table 2). K8, despite showing no binding at any AR subtype (Lagarias *et al.*, 2018), showed a reduced cAMP accumulation. We tested K8 for agonist activity at the A₃R but was found to be no different to DMSO (Supplementary Fig. 3).

A number of compounds previously documented (K5, K9, K21, K22 and K24; Lagarias *et al.*, 2018) or determined in this study (K26, K27 and K34) to have micromolar binding affinity for A₃R showed no activity in our functional screen (Table 1, Supplementary Table 1). These compounds, with a K_i in the low micromolar range, were further tested to ensure our functional screen was robust. In addition, compound K11 with a previously determined low micromolar K_i and a similar structure to the active K10 and K32 was also tested at the higher concentration. Full inhibition curves of NECA in the presence or absence of tested compounds (1 μM or 10 μM) were determined in A₃R Flp-In CHO cells (Supplementary Fig. 4,

Supplementary Table. 3). All nine compounds (K5, K9, K11, K21, K22, K24, K26, K27 and K34) reduced the NECA potency at the highest tested concentration (10 μ M) but showed no effect at 1 μ M and thus appear to be low potency antagonists at the A₃R.

AR subtype selectivity and specificity

Stimulation of A₃R Flp-In CHO or CHO-K1 cells expressing one of the remaining AR subtypes (A₁R, A_{2A}R or A_{2B}R) with a single high concentration of antagonist (10 μ M) and increasing concentrations of NECA identified K10, K17, K18 and K25 as A₃R selective antagonists, with no apparent antagonism at the remaining AR subtypes (Fig. 1). K20 and K23 were antagonists at both the A₁R and A₃R (Fig. 1 and Table 2). K1, K20 and K23 showed weak antagonism of the A_{2A}R and K32 was the only tested antagonist which showed any A_{2B}R activity. These selectivity findings agree with our previously published radioligand binding data (Lagarias *et al.*, 2018) and are summarised in Table 2.

Characterisation of competitive antagonists at the A₃R

All eight A₃R antagonists were confirmed to antagonise IB-MECA agonism (Fig. 2 and Table 3) and NECA agonism (Supplementary Fig. 5 and Supplementary Table 4) in a concentration-dependent manner. Schild analysis of the antagonism of both NECA or IB-MECA stimulated cAMP inhibition characterised K10, K17, K18, K20, K23 and K32 as competitive antagonists at the A₃R with a slope not significantly different from unity (Supplementary Fig. 5 and Fig. 2). Interestingly, the slope deviated from unity for K1 (in experiments looking at competition with NECA but not IB-MECA) and K25 suggesting a more complicated mechanism of antagonism at the A₃R is in play. K20 and K23 were also characterised as competitive antagonists at the A₁R with a Schild slope not significantly different from unity (Supplementary Fig. 6 and Supplementary Table 5).

When comparing the activity of A₃R selective antagonists (K10, K17, K18 and K25), K18 was the most potent, showed A₃R specificity and greater A₃R binding affinity (Table 2). It should be noted however, that the original competition binding experiments that identified the panel of antagonist was performed using [³H]HEMADO (Lagarias *et al.*, 2018). To ensure that the different ligand used in our studies was not influencing our characterisation of the compounds we assessed the ability of K18 to antagonise cAMP inhibition by HEMADO at the A₃R and compared its potency to K17 (Supplementary Fig. 7 and Table 6). As we observed for both NECA and IB-MECA, K18 remained the most potent antagonist at the A₃R and we propose it as our lead compound.

We wanted to determine if our lead A₃R antagonist, K18, could also reduce the potency of IB-MECA when an alternative downstream signalling component was measured; ERK1/2 phosphorylation (Fig. 3). In line with previously reported findings (Schulte and Fredholm, 2002), agonists at the A₃R caused an increase in ERK1/2 phosphorylation after 5 minutes, with IB-MECA 10-fold more potent than NECA (Supplementary Fig. 8). As previously reported (Graham *et al.*, 2001, Schulte and Fredholm, 2002), this was entirely G_{i/o}-mediated, as demonstrated by the abolished pERK1/2 level in PTX treated A₃R Flp-InTM-CHO stimulated with NECA/IB-MECA (Supplementary Fig. 8). The pERK1/2 level following Phorbol 12-myristate 13-acetate (PMA) stimulation was entirely unaffected by PTX treatment (Supplementary Fig. 8). Perhaps unsurprisingly, K18 was able to antagonise A₃R-mediated

phosphorylation of ERK1/2 with the antagonist potency (pA_2 values) not significantly different compared to the cAMP-inhibition assay (Fig. 3C).

A₃R constitutive activity and inverse agonism

A number of GPCRs have been described to have constitutive activity whereby the receptor is active in the absence of agonist: existing at equilibrium in an active (R^*) and an inactive (R) state, i.e the two-state model of agonism. These findings alter the classical concept of competitive antagonism giving rise to the term inverse agonist: ligands/compounds which preferably bind to the R state, decreasing the level of constitutive activity (Giraldo *et al.*, 2007). The A_3R , when expressed in Flp-InTM-CHO cells, displays constitutive activity; as demonstrated by a reduction in 10 μ M forskolin stimulated cAMP accumulation when compared to Flp-InTM-CHO cells (Supplementary Fig. 9). All eight characterised A_3R antagonists showed a concentration dependent inverse agonism of the A_3R when compared to DMSO control (Fig. 2). This was also found to be the case for DPCPX, K20 and K23 at the A_1R (Supplementary Fig. 10). Notably, DMSO showed a concentration-dependent elevation in cAMP accumulation above that of forskolin alone.

MD simulation of the binding mode of K18 at A₃R

We next sought to investigate the potential binding pose of K18 within the A_3R orthosteric site. Building upon our previous studies where we have generated a homology model of the A_3R , K18 was docked into the orthosteric site of the A_3R using the GoldScore scoring function and the highest scoring pose was inserted in a hydrated POPE bilayer. The complex was subjected to MD simulations in the orthosteric binding site of A_3R with Amber14ff for 100 ns and the trajectory analyzed for protein-ligand interactions. We identified a potential binding pose of K18 within the established orthosteric A_3R binding pocket (Fig. 4). A number of residues were identified as potentially important in binding of K18 within the orthosteric binding site and included L90^{3,32}, F168^{5,29}, V169^{5,30}, M177^{5,40}, L246^{6,51}, I249^{6,54}, N250^{6,55} and L264^{7,34} (Fig. 4A). The MD simulations showed that K18 forms hydrogen bonds, van der Waals and π - π interactions inside the orthosteric binding site of A_3R (Fig. 4A). More specifically, MD simulations showed that the 3-(dichlorophenyl) group can be positioned close to V169^{5,30}, M177^{5,40}, I249^{6,54} and L264^{7,34} of the A_3R orthosteric binding site forming attractive vdW interactions. The isoxazole ring is engaged in an aromatic π - π stacking interaction with the phenyl group of F168^{5,29} (Fig. 4A). The thiazole ring is oriented deeper into the receptor favoring interactions with L246^{6,51}, L90^{3,32} and I268^{7,39}. Hydrogen bonding interactions can be formed between: (a) the amino group of the carbonyloxycarboximidamide molecular segment and the amide side chain of N250^{6,55}; (b) the nitrogen or the sulfur atom of the thiazole ring and N250^{6,55} side chain (Fig. 4A). For structural comparison and insight, we also modelled K5 and K17 binding at the A_3R given the structural similarity: K5 when compared to K17 and K18 possess one and two chlorine atoms attached to the phenyl ring, respectively (Fig. 4B and C).

Molecular Mechanics-Poisson Boltzmann Surface Area (MM-PBSA) calculations validate binding pose of K18

We observed the order of potency and binding affinity of the three related compounds K5, K17 and K18, which differ in the number of chlorine atoms connected with the phenyl ring of the phenyl-isoxazole system (0Cl < 1Cl < 2Cl, respectively), as K5 < K17 < K18. The MD simulations for 100 ns showed that these compounds adopted a similar binding position at the A_3R orthosteric binding site (Fig. 4, A-C). The MM-PBSA method was applied in the MD simulation trajectories of the compounds to calculate their binding free energies (ΔG_{eff}) and

evaluate the energetic contributions for their binding (Table 4). The calculated ranking in the binding free energies were in agreement with experimental differences in potencies. Binding free energies (ΔG_{eff}) is calculated as the difference in energetic components between the complex, the apoprotein and the ligand. These components include the difference in electrostatic energy of binding interactions (E_{elec}), the difference in the van der Waals energy of binding interactions (E_{vdW}) and the difference in the solvation energy (ΔG_{solv}) (Table 4). The calculations suggested that the major difference between the energetic components of ΔG_{eff} values for K5, K17 and K18 is on the solvation energies. The two chlorine atoms make K18 more lipophilic and reduce the energy required to transfer the compound from solution to the binding area, increasing the free energy of binding and activity compared to K17 and K5. Interestingly, following MD simulations of the unpublished compounds (K26, K27, K29-K34 and K36-K39) we observed that compounds K26, with a *o*-diphenylcarbonyl, had low micromolar A_3R binding affinities (Supplementary Table 1) and according to the MD simulations of K26 in complex with A_3R (Supplementary Fig. 11) had a similar binding pose to that of K18 (Fig. 4). However, in our functional assays, K26 (and K34, which also had a *o*-diphenylcarbonyl and low micromolar binding) showed weak antagonistic potency below the concentration of 1 μM (Supplementary Fig. 3) suggesting a more complex binding mode is present. We observed that the *p*-substitution in compounds K29 and K36-38 was not favorable for binding at all since this led to a loss of the van der Waals interaction with the hydrophobic area of the A_3R towards TM5 and TM6; as was demonstrated in MD simulations for K36 (Supplementary Fig. 11).

Finally, we also examined how the activity was affected when the 4-thiazolyl in the mid-range antagonist K17 was changed to 2-,3- or 4-pyridyl in compounds K32, K10, K11 which bind to A_3R (Table 1). We found antagonistic activity only for compounds K32 and K10; compared to K11, in compounds K32 and K10 the pyridine nitrogen can interact with N250^{6.55} due to their proximate positions in binding conformation (see Fig. 4B for K17). This interaction appears to be preserved with both the 2-,3-pyridyl groups but lost when the nitrogen is in the 4-position. Thus, while we have been able to identify compounds that are structurally able to mimic some of the features of compound K18 (and its derivatives K17 and K5), K18 remains the most potent antagonist present within this study.

Experimental evaluation of the binding mode of K18 at A_3R

The potential binding site of our lead A_3R selective antagonist, K18, was investigated through the use of point mutations as an experimental approach to give insight into structure-function relationships. The determination of critical residues for antagonist binding becomes particularly difficult in the case of competitive antagonists whereby important amino acids are likely overlapping with those for agonist binding. Through performing Schild analysis, whereby the pA_2 is independent of agonist, we were able to experimentally determine the effect of receptor mutation on antagonist binding. Whereas an increase in the pA_2 for a particular mutant when compared to WT suggested the antagonist was more potent, a decrease indicated a reduced potency. Of the identified residues predicted to mediate an interaction between K18 and the A_3R , the ones which showed (according to the MD simulations) the most frequent and the most important contacts were chosen for investigation and included amino acids L90^{3.32}, F168^{5.29}, V169^{5.30}, M177^{5.40}, L246^{6.51}, I249^{6.54}, N250^{6.55}, L264^{7.34} and I268^{7.39} (Fig. 4). Site-directed mutagenesis was performed replacing each residue with an alanine and expressed then in the Flp-In-CHOTM cells lines. Each mutant was then screened for their ability to suppress forskolin-induced cAMP accumulation in response to NECA/IB MECA stimulation in the presence and absence of K18.

Mutation of residues F168^{5.29}, L246^{6.51}, N250^{6.55} and I268^{7.39} abolished agonist induced suppression of forskolin-induced cAMP accumulation and were discontinued in this study (Stamatis *et al.*, 2019, in preparation). Both L90A^{3.32} and M177A^{5.40} showed a significantly decreased NECA and IB-MECA potency. L264A^{7.34} showed a slight decrease in IB-MECA potency whereas the potency of NECA was similar to WT. Whereas the NECA stimulated cAMP inhibition in V169A^{5.30} or I249A^{6.54} expressing Flp-In CHOs was comparable to WT, the IB-MECA stimulated cAMP inhibition was enhanced in potency (Table 5). Mutation of V169^{5.30} to glutamate, the amino acid present in the remaining three AR subtypes, enhanced both NECA and IB-MECA potency.

Schild analysis of K18 at WT and mutant A₃R

The pA₂ values obtained through conducting Schild analysis of K18 at WT and mutant A₃R were compared in order to determine the potential antagonist binding site (Fig. 5, Table 5). The pA₂ value for I249A^{6.54} A₃R was similar to WT, whereas M177A^{5.40} and V169A^{5.30} were significantly smaller. Interestingly we found an increase in the pA₂ for L90A^{3.32} and L264A^{7.34} when compared to WT, suggesting an enhanced ability of K18 to act as an antagonist. Our confidence in the obtained pA₂ values for K18 was enhanced by testing with NECA and IB-MECA at an A₃R mutant which caused enhanced activity (L90A^{3.32}). As would be expected, the pA₂ values for this mutant was not significantly different between agonists, confirming agonist independence (Supplementary Fig. 12). These experimental findings are reflected in our final binding pose of K18 at the WT A₃R (Fig. 4).

Kinetics of A₃R antagonists determined through BRET

BRET techniques have been successfully used to determine the real time kinetics of ligand binding to GPCRs (Stoddart *et al.*, 2018, Sykes *et al.*, 2019). In BRET ligand-binding experiments, we investigated the ability of the selective A₃R antagonist MRS 1220, K5, K17 or K18 to inhibit specific binding of the fluorescent A₃R antagonist CA200645 to Nluc-A₃R. The kinetic parameters for CA200645 at Nluc-A₃R were initially determined as K_{on} (k₁) = 2.86 ± 0.89 × 10⁷ M⁻¹, K_{off} (k₂) = 0.4397 ± 0.014 min⁻¹ with a K_D of 17.92 ± 4.45 nM. (Supplementary Fig 13). Our MRS 1220 kinetic data was fit with the original 'kinetic of competitive binding' model (Motulsky and Mahan, 1984; built into GraphPad Prism 8.0) with a determined K_{on} (k₃) and K_{off} (k₄) rate of 3.25 ± 0.28 × 10⁸ M⁻¹ min⁻¹ and 0.0248 ± 0.005 min⁻¹, respectively. This gave a residence time (RT) (RT = 1/K_{off}) of 40.32 min. It was noticed in the analysis for K5, K17 and K18 that the fit in some cases was ambiguous (Regression with Prism 8: "Ambiguous", 2019) and/or the fitted value of the compound dissociation rate constant was high (k₄ > 1 min⁻¹, corresponding to a dissociation t_{1/2} of < 42 sec). In order to determine the reliability of the fitted k₄ value, data were also analysed using an equation that assumes compound dissociation is too rapid for the dissociation rate constant to be determined reliably and the fits to the two equations compared ("Kinetics of competitive binding, rapid competitor dissociation", derived in the Appendix I). This model allowed estimate of the equilibrium binding affinity of the compound (K_i) but not the binding kinetics of K5, K17 and K18 (Supplementary Fig. 14 and Table 4). These pK_i values were found to be similar to those calculated through fitting the Cheng-Prusoff equation (Cheng and Prusoff, 1973) and notably, the order of affinity for K5, K17 and K18 reflected that determined through Schild analysis and previously published radioligand binding (Table 4).

DISCUSSION

In silico structure-based drug design efforts in ligand discovery, using molecular docking calculations, have proven to be highly successful (Meng *et al.*, 2011). The broad and similar orthosteric binding site of ARs makes the determination of AR subtype selective compound a challenging task. Indeed, given the similarity between ARs orthosteric binding sites, the search for an AR subtype specific compound often leads to compounds active at more than one of the AR subtypes (Kolb *et al.*, 2012). Given that AR subtypes play distinct roles throughout the body, obtaining highly specific receptor antagonists and agonists is crucial. Here, we presented the pharmacological characterisation of eight A₃R antagonists determined through virtual screening. Of these eight compounds, K10, K17, K18, K20, K23 and K32 were determined to be competitive. Whereas K20 and K23 were antagonists at both the A₁R and A₃R, K10, K17, K18 and K25 were A₃R selective antagonists. Indeed, we found no functional activity, or indeed binding affinity (< 30 μM), at the other AR subtypes.

K1, K20 and K23 showed weak antagonism of the A_{2A}R and K32 was the only tested antagonist which showed A_{2B}R antagonistic potency. These selectivity findings were in agreement with our radioligand binding data (presented here and in Lagarias *et al.*, 2018 for K1-25, K28 and K35). However, a number of compounds previously determined to have micromolar binding affinity for A₃R (K5, K9, K21, K22, K24, K26, K27 and K34), showed no antagonistic potency in our initial functional screen. Further testing confirmed that these compounds were low potency antagonists and, although supporting the previously published radioligand binding data, confirmed the need for functional testing: not all compounds with binding affinity showed high functional potency.

We showed the A₃R, when expressed in Flp-InTM-CHO cells, displays constitutive activity. Compounds which preferably bind to the inactive (R) state, decreasing the level of constitutive activity (Giraldo *et al.*, 2007) and in the case of a G_{i/o}-coupled GPCR leading to an elevated cAMP, are referred to as inverse agonists. All eight characterised A₃R antagonists and both characterised A₁R antagonists (K20 and K23) were found to act as inverse agonists. We also reported an elevation in cAMP accumulation when cells were stimulated with DMSO, which was concentration-dependent. Given that even low concentrations of DMSO has been reported to interfere with important cellular processes (Tunçer *et al.*, 2018), the interpretation of this data should be made with caution. The initial virtual screening described in Lagarias *et al.*, 2018 was carried out using a combination of a ligand-based and structure-based strategy and the experimental structure of A_{2A}R in complex with the antagonist ZM241385 (PDB ID 3EML) (Jaakola *et al.*, 2008), described as A_{2A}R selective antagonist and inverse agonist (Lebon *et al.*, 2011). Our high hit rate for A₃R selective antagonist appears counter-intuitive since the ligand-based virtual screening tool Rapid Overlay of Chemical Structures (ROCS) was used to predict structures similar to ZM241385 (Lagarias *et al.*, 2018). Indeed, ZM241385 has little affinity for A₃R and 500- to 1000-fold selectivity for A_{2A}R over A₁R. However, as has been previously reported, the search for an AR subtype specific compound often leads to compounds active at multiple AR subtypes (Kolb *et al.*, 2012), likely due to their similar binding site.

We hypothesize that the presence of a chloro substituent in the phenyl ring of 3-phenylisoxazole favors A₃R affinity and activity, as following 0Cl < 1Cl < 2Cl i.e. K5 < K17 < K18.

This theory is supported by both our radioligand binding, NanoBRET ligand-binding and functional data which determine the relative potency and affinity of the three related compounds K5, K17 and K18 as $K5 < K17 < K18$. The MD simulations showed that these compounds adopted a similar binding mode at the A₃R orthosteric binding site, but the free-energy calculations showed that the two chlorine atoms in K18 increases its lipophilicity, thus allowing it to more efficiently leave the solution state and enter the highly lipophilic binding area.

For the first time, we demonstrate the utilisation of a new model which expands on the 'Kinetic of competitive binding' model (Motulsky and Mahan, 1984; built into Prism) for fitting fast kinetics data obtained from NanoBRET experiments and assumes the unlabelled ligand rapidly equilibrates with the free receptor. Very rapid competitor dissociation can lead to failure of the fit, eliciting either an ambiguous fit (Regression with Prism 8: "Ambiguous", 2019) or unrealistically large K₃ and K₄ values. Whereas we were able to successfully fit the MRS 1220 kinetic data with the Motulsky and Mahan model due to its slow dissociation, fitting of K5, K17 and K18 kinetic data with this model often resulted in an ambiguous fit. Our new model, assuming fast compound dissociation, successfully fit the data and allowed the determination of binding affinity. In the cases where the data was able to fit the Motulsky and Mahan model, the dissociation constant was higher (of the order of 1 min⁻¹), indicating rapid dissociation. Although we found nearly a 10-fold differences in determined binding affinity for MRS 1220, K5, K17 and K18 between BRET ligand binding and radioligand binding assays, we demonstrate the order of affinity remains consistent. Indeed, this was seen across all three experimental approaches: Schild analysis, NanoBRET ligand-binding assay and radioligand binding.

Our MD simulations showed the potential binding site of K18, our most potent and selective A₃R antagonist, within the A₃R orthosteric binding area (Fig. 4A). Here, K18 is stabilised through hydrogen bonding interactions between the amino group and thiazole ring of the ligand and the amide side chain of N250^{6.55}. In addition, the dichloro-phenyl ring can be oriented to the unique lipophilic area of A₃R including V169^{5.30}, M177^{5.40}, I249^{6.54} and L264^{7.34} stabilized in that cleft through attractive van der Waals interactions; K18 is further stabilized through π - π aromatic stacking interactions between isoxazole ring and the phenyl group of F168^{5.29} and the thiazole group is oriented deeper into the receptor favoring interactions with L246^{6.51} and L90^{3.32} and possibly with I268^{7.39}. In combination with our mutagenesis data, the final binding pose of K18 appears to be within the orthosteric binding site, involving residues previously described to be involved in binding of A₃R compounds (Arruda *et al.*, 2017). We reported no detectable G_{i/o} response following co-stimulation with forskolin and NECA or IB-MECA for A₃R mutants F168A^{5.29}, L246A^{6.51}, N250A^{6.55} and I268A^{7.39} (Stamatis *et al.*, 2019, in preparation). These findings are in line with previous mutagenesis studies investigating residues important for agonist and antagonist binding at the human A₃R (Gao *et al.*, 2002, May *et al.*, 2012). L90A^{3.32}, V169A^{5.30}, M177A^{5.40}, I249A^{6.54} and L264A^{7.34} A₃R all showed a detectable G_{i/o} response when stimulated with agonists (Stamatis *et al.*, 2019).

Through performing Schild analysis, we were able to experimentally determine the effect of receptor mutation on antagonist affinity for L90A^{3.32}, V169A/E^{5.30}, M177A^{5.40}, I249A^{6.54} and L264A^{7.34} A₃R. The pA₂ value for I249A^{6.54} A₃R was similar to WT, whereas M177A^{5.40} and V169A^{5.30} were significantly smaller suggesting these residues appear to be involved in K18 binding. Interestingly we found an increase in the pA₂ for L90A^{3.32} and L264A^{7.34} when

compared to WT, suggesting an enhanced ability of K18 to act as an antagonist. Further evidence was provided by the MM-PBSA calculations which were in agreement, based on the proposed binding model, between the calculated binding free energy by congeners of K18 having one or no chlorine atoms, i.e. compounds K17 and K5, and binding affinities and antagonistic potency. Importantly, substitution of the 1,3-thiazole ring in K17 with either a 2-pyridyl ring (K32) or a 3-pyridyl ring (K10) but not a 4-pyridyl ring (K11) maintained A₃R antagonistic potency. Although we have not directly determined the effects of similar pyridyl ring substitutions on the higher affinity antagonist K18, we suspect there would be no significant increase in the potency of K18 given the small changes we observed for K17.

In conclusion, through pharmacological characterisation of a number of potential A₃R antagonists, this study has determined K18 as a specific (<1 µM) A₃R competitive antagonist. Our mutagenic studies, supported by MD simulations, identified the residues important for K18 binding are located within the orthosteric site of the A₃R. Importantly, the absence of a chloro substituent, as is the case in K5, led to affinity loss. We suggest that the high affinity subtype selectivity of K18 makes it a molecule to begin detailed SAR and represents a useful tool compound that warrants further assessment for its therapeutic potential.

MATERIALS AND METHODS

Cell culture and Transfection

Cell lines were maintained using standard subculturing routines as guided by the European Collection of Cell Culture (ECACC) and checked annually for mycoplasma infection using an EZ-PCR mycoplasma test kit from Biological Industries (Kibbutz Beit-Haemek, Israel). All procedures were performed in a sterile tissue culture hood using aseptic technique and solutions used in the propagation of each cell line were sterile and pre-warmed to 37°C. All cells were maintained at 37°C with 5% CO₂, in a humidified atmosphere. CHO-K1-A₁R or CHO-K1-A₃R cells were routinely cultured in Hams F-12 nutrient mix (21765029, Thermo Fisher Scientific) supplemented with 10% Foetal bovine serum (FBS) (F9665, Sigma-Aldrich). Flp-In-CHO cells purchased from Thermo Fisher Scientific (R75807) were maintained in Hams F-12 nutrient mix supplemented with 10% FBS containing 100 µg/mL Zeocin™ Selection Antibiotic (Thermo Fisher Scientific).

Stable Flp-In-CHO cell lines were generated through co-transfection of the pcDNA5/FRT expression vector (Thermo Fisher Scientific) containing the gene of interest and the Flp recombinase expressing plasmid, pOG44 (Thermo Fisher Scientific). Transfection of cells seeded in a T25 flask at a confluency of ≥80% was performed using TransIT®-CHO Transfection Kit (MIR 2174, Mirus Bio), in accordance with the manufacturer's instructions. Here, a total of 6 µg of DNA (receptor to pOG44 ratio of 1:9) was transfected per flask at a DNA:Mirus reagent ratio of 1:3 (w/v). 48 hours post-transfection, selection using 600 µg/mL hygromycin B (Thermo Fisher Scientific), concentration determined through performing a kill curve, was performed for two days prior to transferring the cells into a fresh T25 flask. Stable Flp-In-CHO cell lines expressing the receptor of interest were selected using 600 µg/mL hygromycin B whereby the media was changed every two days. Successful mutant cell line generation for non-signalling mutants were confirmed by Zeocin™ sensitivity (100 µg/mL).

Constructs

The human A₃R originally in pcDNA3.1+ (ADRA3000000, cdna.org) was cloned into the pcDNA5/FRT expression vector and co-transfected with pOG44 to generate a stable Flp-In-CHO cell line. Mutations within the A₃R were made using the QuikChange Lightning Site-Directed Mutagenesis Kit (Agilent Technologies) in accordance with the manufacturer's instructions. All oligonucleotides used for mutagenesis were designed using the online Agilent Genomics 'QuikChange Primer Design' tool (Supplementary Table 7) and purchased from Merck. All constructs were confirmed by in-house Sanger sequencing.

Compounds

Adenosine, NECA (5'-(N-ethylcarboxamido)adenosine), IB-MECA (1-deoxy-1-[6-[[[(3-iodophenyl)methyl]amino]-9H-purin-9-yl]-N-methyl-β-D-ribofuranuronamide), 2-(1-hexynyl)-N⁶-methyladenosine (HEMADO), 8-cyclopentyl-1,3-dipropylxanthine (DPCPX) and MRS 1220 (N-[9-chloro-2-(furan-2-yl)-[1,2,4]triazolo[1,5-c]quinazolin-5-yl]-2-phenylacetamide) were purchased from Sigma-Aldrich and dissolved in dimethyl-sulphoxide (DMSO). PMA was purchased from Sigma-Aldrich. Compounds under investigation were purchased from e-molecules and dissolved in DMSO.

cAMP accumulation assay

For cAMP accumulation (A_{2A}R and A_{2B}R) or inhibition (A₁R or A₃R) experiments, cells were harvested and re-suspended in stimulation buffer (PBS containing 0.1% BSA and 25 μM rolipram) and seeded at a density of 2,000 cells per well of a white 384-well Optiplate and stimulated for 30 minutes with a range of agonist concentrations. In order to allow the A₁R/A₃R mediated G_{i/o} response to be determined, co-stimulation with forskolin, an activator of AC (Zhang *et al.*, 1997), at the indicated concentration (depending on cell line) was performed. For testing of potential antagonists, cells received a co-stimulation stimulated with forskolin, agonist and compound/DMSO control. cAMP levels were then determined using a LANCE® cAMP kit as described previously (Knight *et al.*, 2016). In order to reduce evaporation of small volumes, the plate was sealed with a ThermalSeal® film (EXCEL Scientific) at all stages.

Phospho-ERK assay

ERK1/2 phosphorylation was measured using the homogeneous time resolved fluorescence (HTRF)® Phospho-ERK (T202/Y204) Cellular Assay Kit (Cisbio Bioassays, Codolet, France) two-plate format in accordance with the manufacturer's instructions. A₃R expressing Flp-In-CHO were seeded at a density of 2,000 cells per well of a white 384-well Optiplate and stimulated with agonist and test compounds for 5 minutes at 37°C. Plate reading was conducted using a Mithras LB 940 (Berthold technology). All results were normalised to 5 minutes stimulation with 1 μM PMA, a direct protein kinase C (PKC) activator (Jiang and Fleet, 2012). To determine if the measured pERK1/2 level was G_i-mediated, we treated cells with Pertussis toxin (PTX) (Tocris Biosciences) for 16 hours at 100 ng/mL prior to pERK assay.

Radioligand Binding

All pharmacological methods followed the procedures as described in the literature (Klotz *et al.*, 1998). In brief, membranes for radioligand binding were prepared from CHO cells stably transfected with hAR subtypes in a two-step procedure. In the first step, cell fragments and nuclei were removed at 1000 x g and then the crude membrane fraction was sedimented from the supernatant at 100000 x g. The membrane pellet was resuspended in the buffer used for the respective binding experiments and it was frozen in liquid nitrogen and stored at -80°C. For radioligand binding at the A₁R, 1 nM [³H]CCPA was used, for A_{2A}R 10 nM [³H]NECA and

for A₃R 1 nM [³H]HEMADO. Non-specific binding of [³H]CCPA was determined in the presence of 1 mM theophylline and in the case of [³H]NECA and [³H]HEMADO 100 μM R-PIA was used. K_i values from competition experiments were calculated using Prism (GraphPad Software, La Jolla, CA, U.S.A.) assuming competitive interaction with a single binding site. The curve fitting results (see Fig. 8 in Lagarias et al. 2018) showed R² values ≥ 0.99 for all compounds and receptors, indicating that the used one-site competition model assuming a Hill slope of n=1 was appropriate.

Determining K_{on} and K_{off} rates of A₃R antagonists

Through the use of NanoBRET, real-time quantitative pharmacology of ligand-receptor interactions can be investigated in living cells. CA200645, a high affinity AR xanthine amine congener (XAC) derivative containing a polyamide linker connected to the BY630 fluorophore, acts as a fluorescent antagonist at both A₁R and A₃R with a slow off-rate (Stoddart *et al.*, 2012). Using an N-terminally NanoLuc (Nluc)-tagged A₃R expressing cell line, competition binding assays were conducted. The kinetic data was fitted with the 'kinetic of competitive binding' model (Motulsky and Mahan, 1984; built into Prism) to determine affinity (pK_i) values and the association rate constant (K_{on}) and dissociation rates (K_{off}) for unlabelled A₃R antagonists. This model resulted in several cases in an ambiguous fit (Regression with Prism 8: "Ambiguous", 2019). We developed a new model which expands on the 'kinetic of competitive binding' model to accommodate very rapid competitor dissociation, assuming the unlabelled ligand rapidly equilibrates with the free receptor. This method allows determination of compound affinity (pK_i) from the kinetic data.

Filtered light emission at 450 nm and > 610 nm (640-685 nm band pass filter) was measured using a Mithras LB 940 and the raw BRET ratio calculated by dividing the 610 nm emission with the 450 nm emission. Here, Nluc on the N-terminus of A₃R acted as the BRET donor (luciferase oxidizing its substrate) and CA200645 acted as the fluorescent acceptor. CA200645 was used at 25 nM, as previously reported (Stoddart *et al.*, 2015). BRET was measured following the addition of the Nluc substrate, furimazine (0.1 μM). Nonspecific binding was determined using a high concentration of unlabelled antagonist, MRS 1220 (10 nM), for Nluc-A₃R.

Receptor binding kinetics data analysis

Specific binding of tracer vs time data was analysed using the Motulsky and Mahan method (Motulsky and Mahan, 1984; built into Prism) to determine the test compound association rate constant and dissociation rate constant. Data were fit to the "Kinetics of competitive binding" equation in Prism 8.0 (GraphPad Software Inc, San Diego, CA):

$$[RL]_t = \frac{N[L]k_1}{K_F - K_S} \left[\frac{k_4(K_F - K_S)}{K_F K_S} - \frac{k_4 - K_S}{K_S} e^{-K_S t} + \frac{k_4 - K_F}{K_F} e^{-K_F t} \right]$$

where,

$$K_F = 0.5 \left\{ K_A + K_B + \sqrt{(K_A - K_B)^2 + 4[L][I]k_1 k_3} \right\}$$

$$K_S = 0.5 \left\{ K_A + K_B - \sqrt{(K_A - K_B)^2 + 4[L][I]k_1 k_3} \right\}$$

$$K_A = [L]k_1 + k_2$$

$$K_B = [I]k_3 + k_4$$

$[RL]_t$ is specific binding at time t , N the B_{\max} , $[L]$ the tracer concentration, $[I]$ the unlabelled competitor compound concentration, k_1 the tracer association rate constant, k_2 the tracer dissociation rate constant, k_3 the compound association rate constant and k_4 the compound dissociation rate constant.

Data were also analysed using an equation that assumes compound dissociation is too rapid for the dissociation rate constant to be determined reliably and the fits to the two equations compared (“Kinetics of competitive binding, rapid competitor dissociation”, derived in the Appendix I, Supplementary material). This equation assumes rapid equilibration between compound and receptor and consequently provides an estimate of the equilibrium binding affinity of the compound (K_i) but not the binding kinetics of the compound. The equation is,

$$[RL]_t = \frac{N[L]k_1(1 - \rho_I)}{k_{obs,+I}} (1 - e^{-k_{obs,+I}t})$$

where ρ_I is fractional occupancy of receptors not bound by L :

$$\rho_I = \frac{[I]}{K_I + [I]}$$

and $k_{obs,+I}$ is the observed association rate of tracer in the presence of competitor, defined as,

$$k_{obs,+I} = [L]k_1(1 - \rho_I) + k_2$$

The fits to the two equations were compared statistically using a partial F-test in Prism 8 (Motulsky, 2019).

Data and Statistical analysis

All *in vitro* assay data was analysed using Prism 8.0 (GraphPad software, San Diego, CA), with all dose-inhibition or response curves being fitted using a 3-parameter logistic equation to calculate response range or E_{\max} and IC/EC_{50} . Dose-inhibition/dose-response curves were normalised to either forskolin response or forskolin inhibition (A_1R and A_3R), relative to NECA/IB-MECA. In the case of pERK1/2 response, normalisation was performed to PMA.

Schild analysis was performed to obtain pA_2 values (the negative logarithm to base 10 of the molar concentration of an antagonist that makes it necessary to double the concentration of the agonist to elicit the original submaximal response obtained by agonist alone (Schild, 1947)) for the potential antagonists. In cases where the Schild slope did not differ significantly from unity, the slope was constrained to unity giving an estimate of antagonist affinity (pK_B). pA_2 and pK_B coincide when the slope is exactly unity. The pA_2 values obtained through conducting Schild analysis of K18 at WT and mutant A_3R were compared in order to indicate important residues involved in K18 binding.

The data and statistical analysis comply with the recommendations on experimental design and analysis in pharmacology (Curtis *et al.*, 2018). Statistical significance (*, $p < 0.05$; **, $p < 0.01$; ***, $p < 0.001$; ****, $p < 0.0001$) was calculated using a one-way ANOVA with a Dunnett's post-test for multiple comparisons or Students' t-test, as appropriate. Compounds taken forwards for further experiments after initial screening were identified as having the highest statistical significance (P value of 0.001 (***) or < 0.0001 (****)). All statistical analysis was performed using Prism 8.0 on data which were acquired from experiments performed a minimum of five times, conducted in duplicate.

Computational biochemistry

MD simulations

Preparation of the complexes between A₃R and K5, K17 or K18 was based on a homology model of A_{2A}R (see Appendix II in Supplementary material). Each ligand-protein complex was embedded in hydrated POPE bilayers. A simulation box of the protein-ligand complexes in POPE lipids, water and ions was built using the System Builder utility of Desmond (Desmond Molecular Dynamics System, version 3.0; D.E. Shaw Res. New York, 2011; Maest. Interoperability Tools, 3.1; Schrodinger Res. New York, 2012.). A buffered orthorhombic system in 10 Å distance from the solute atoms with periodic boundary conditions was constructed for all the complexes. The MD simulations were performed with Amber14 and each complex-bilayer system was processed by the LEaP module in AmberTools14 under the AMBER14 software package (Case *et al.*, 2014). Amber ff14SB force field parameters (Maier *et al.*, 2015) were applied to the protein, lipid14 to the lipids (Dickson *et al.*, 2014), GAFF to the ligands (Wang *et al.*, 2004) and TIP3P (Jorgensen *et al.*, 1983) to the water molecules for the calculation of bonded, vdW parameters and electrostatic interactions. Atomic charges were computed according to the RESP procedure (Bayly *et al.*, 1993) using Gaussian03 (Frisch *et al.*, 2003) and antechamber of AmberTools14 (Case *et al.*, 2014). The temperature of 310 K was used in MD simulations in order to ensure that the membrane state is above the main phase transition temperature of 298 K for POPE bilayers (Koynova and Caffrey, 1998). In the production phase, the relaxed systems were simulated in the NPT ensemble conditions for 100 ns. The visualization of produced trajectories and structures was performed using the programs Chimera (Pettersen *et al.*, 2004) and VMD (Humphrey *et al.*, 1996). All the MD simulations were run on GTX 1060 GPUs in lab workstations or on the ARIS Supercomputer.

MM-PBSA calculations

Relative binding free energies of the complexes between K5, K17 and K18 and A₃R was estimated by the 1-trajectory MM-PBSA approach (Massova and Kollman, 2000). Effective binding energies (ΔG_{eff}) were computed considering the gas phase energy and solvation free energy contributions to binding. For this, structural ensembles were extracted in intervals of 50 ps from the last 50 ns of the production simulations for each complex. Prior to the calculations all water molecules, ions, and lipids were removed, and the structures were positioned such that the geometric center of each complex was located at the coordinate origin. The polar part of the solvation free energy was determined by calculations using Poisson-Boltzmann (PB) calculations (Homeyer and Gohike, 2013). In these calculations, a dielectric constant of $\epsilon_{\text{solute}} = 1$ was assigned to the binding area and $\epsilon_{\text{solute}} = 80$ for water. Using an implicit solvent representation for the calculation of the effective binding energy is

an approximation to reduce the computational cost of the calculations. The binding free energy for each complex was calculated using equation (1)

$$\Delta G_{\text{eff}} = \Delta E_{\text{MM}} + \Delta G_{\text{sol}} \quad (1)$$

In equation (1) ΔG_{eff} is the binding free energy for each calculated complex neglecting the effect of entropic contributions or assuming to be similar for the complexes studied. ΔE_{MM} defines the interaction energy between the complex, the protein and the ligand as calculated by molecular mechanics in the gas phase. ΔG_{sol} is the desolvation free energy for transferring the ligand from water in the binding area calculated using the PBSA model. The terms for each complex ΔE_{MM} and ΔG_{sol} are calculated using equations (2) and (3)

$$\Delta E_{\text{MM}} = \Delta E_{\text{elec}} + \Delta E_{\text{vdW}} \quad (2)$$

$$\Delta G_{\text{sol}} = \Delta G_{\text{P}} + \Delta G_{\text{NP}} \quad (3)$$

In equation (2) ΔE_{elec} and ΔE_{vdW} are the electrostatic and the van der Waals interaction energies, respectively. In equation (3) ΔG_{P} is the electrostatic or polar contribution to free energy of solvation and the term ΔG_{NP} is the non-polar or hydrophobic contribution to solvation free energy. Molecular mechanics energies and the non-polar contribution to the solvation free energy were calculated with the *mmpbsa.pl* module (Miller *et al.*, 2012) of Amber14 (Case *et al.*, 2014).

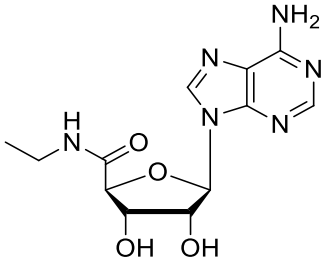
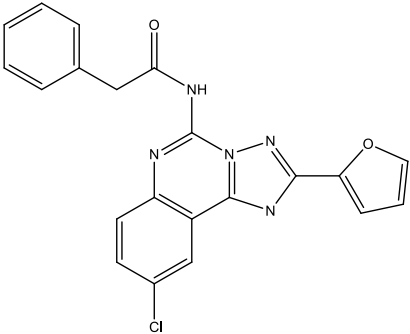
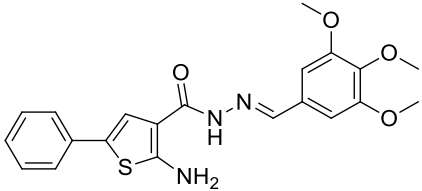
Nomenclature of Targets and Ligands

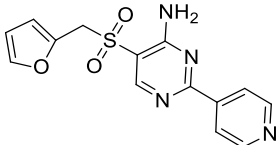
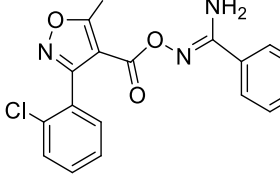
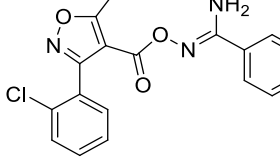
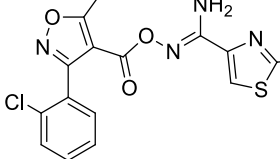
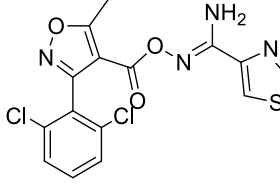
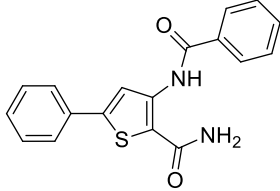
Key protein targets and ligands in this article are hyperlinked to corresponding entries in <http://www.guidetopharmacology.org>, the common portal for data from the IUPHAR/BPS Guide to PHARMACOLOGY (Harding *et al.*, 2018), and are permanently archived in the Concise Guide to PHARMACOLOGY 2017/18 (Alexander *et al.*, 2017).

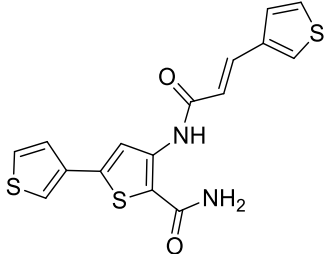
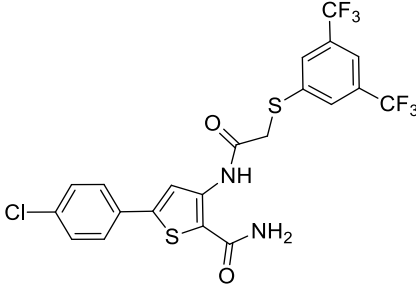
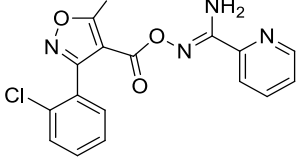
Acknowledgments

We gratefully acknowledge the support of the Leverhulme Trust (KB and GL) and the BBSRC (GL). This research represents part of the Ph.D work of P.L. We thank Chiesi Hellas which supported this research (SARG No 10354) and the State Scholarships Foundation (IKY) for providing a Ph.D fellowship to P.L. (MIS 5000432, NSRF 2014-2020). The work of E.V. is implemented through IKY scholarships programme and co-financed by the European Union (European Social Fund - ESF) and Greek national funds through the action entitled "Reinforcement of Postdoctoral Researchers", in the framework of the Operational Program "Human Resources Development Program, Education and Lifelong Learning" of the National Strategic Reference Framework (NSRF) 2014 – 2020. This work was supported by computational time granted from the Greek Research & Technology Network (GRNET) in the National HPC facility - ARIS - under project IDs pr005010. We would like to thank Stephen Hill, Stephen Briddon and Mark Soave (University of Nottingham) for gifting the Nluc-A₃R cell line and their technical advice. We are also grateful to Sonja Kachler for her technical assistance.

Table 1. Mean cAMP accumulation as measured in Flp-In CHO cells stably expressing A₃R following stimulation with 10 μM forskolin only (DMSO) or 10 μM forskolin, NECA at the predetermined IC₈₀ concentration and 1 μM test compound/MRS 1220/DMSO control. Binding affinities were obtained through radioligand binding assays against the A₁R, A_{2A}R and A₃R.

Compound	Compound name	Chemical structure	cAMP accumulation		Radioligand binding (K _i (μM)) ^c		
			Mean ^a	Mean difference ^b	A ₃ R	A ₁ R	A _{2A} R
	NECA		59.81 ±1.96	-	ND	ND	ND
	DMSO	CH ₃ -SO-CH ₃	100.00 ±1.15 ****	-35.73	ND	ND	ND
	MRS 1220		111.10 ±1.13 ****	-49.44	ND	ND	ND
K1	HTS12884SC ¹		83.26 ±1.68****	-23.45	3.10	>100	2.67

K8	KM03338 ¹		47.13 ±2.09**	12.69	>100	>100	>100
K10	STK300529 ¹		87.73 ±2.78****	-27.91	4.49	>60	>60
K11	SKT323144 ¹		72.88 ±3.24**	-13.07	5.15	>60	30
K17	SPB02734 ¹		88.11 ±2.75****	-28.30	4.16	>30	>60
K18	SPB02735 ¹		103.8 ±1.24****	-43.94	0.89	>100	>100
K20	GK03725 ¹		97.95 ±1.39****	-38.13	0.91	1.09	7.29

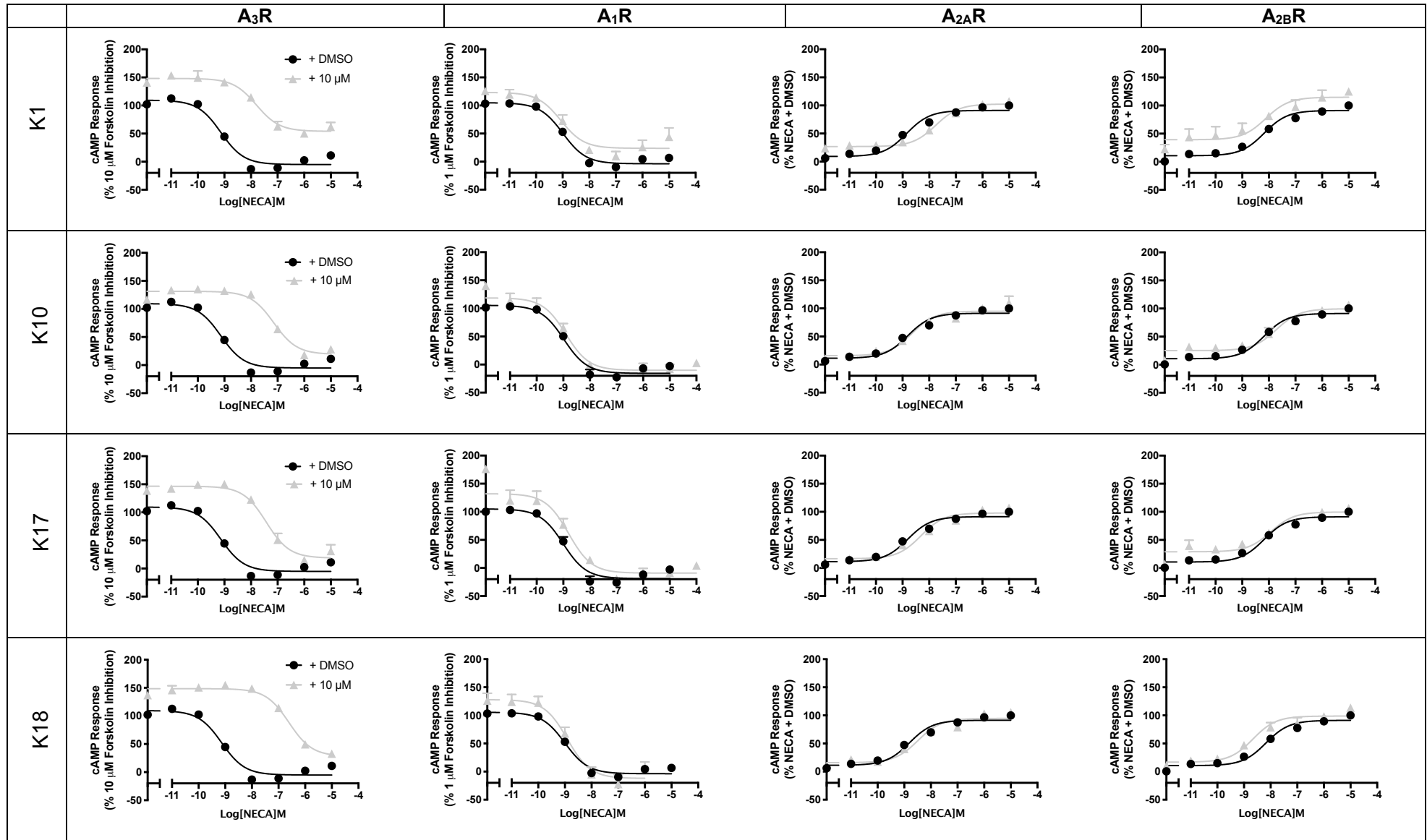
K23	GK01176 ¹		92.27 ±2.62****	-32.46	1.65	1.18	4.69
K25	GK01513 ¹		85.99 ±1.61****	-26.17	1.55	>100	>100
K32	STK323544		86.66 ±2.78****	-26.85	2.40	>100	>100

¹Indicates previously published in Lagarias *et al.*, 2018

^acAMP accumulation mean ± SEM expressed as %10 μM forskolin response where $n \geq 3$ independent experimental repeats, conducted in duplicate. Statistical significance in comparison to co-stimulation with 10 μM forskolin and NECA ('NECA') was determined using one-way analysis of variance with Dunnett's post-test

^bDifference between the mean cAMP accumulation between 'NECA' and each compound expressed as %10 μM forskolin response

^cBinding affinity measured in three independent experiments and where indicated, previously published in Lagarias *et al.*, 2018. Bold denotes binding affinity < 10 μM.



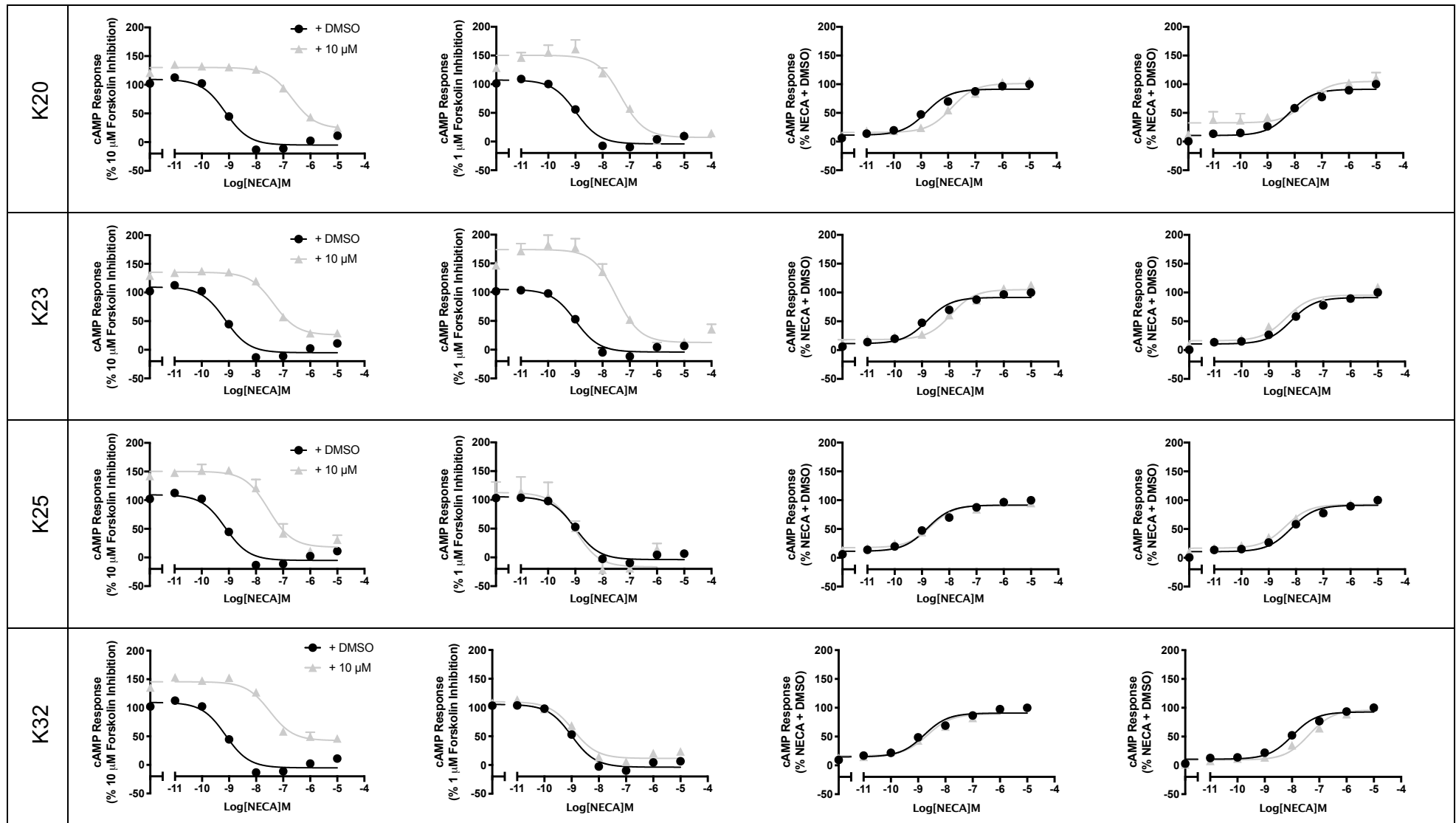


Figure 1. Characterisation of A₃R antagonist at all AR subtypes. A₃R Flp-In CHO cells or CHO-K1 cells (2000 cells/well) stably expressing one of the remaining AR subtypes were exposed to forskolin in the case of G_i-coupled A₁R and A₃R (1 μM or 10 μM, respectively) or DMSO control in the case of G_s-coupled A_{2A}R and A_{2B}R, NECA and test compound (10 μM) for 30 min and cAMP accumulation detected. All values are mean ± SEM expressed as percentage forskolin inhibition (A₁R and A₃R) or stimulation (A_{2A}R and A_{2B}R), relative to NECA. *n* ≥ 3 independent experimental repeats, conducted in duplicate.

Table 2. Potency of NECA stimulated cAMP inhibition or accumulation as determined in Flp-In CHO or CHO-K1 cells expressing one of four ARs subtype (A₃R, A₁R, A_{2A}R or A_{2B}R) and corresponding binding affinity of potential antagonists. Cells stably expressing A₃R, A₁R, A_{2A}R or A_{2B}R were stimulated with forskolin, 10 μM tested compound/DMSO and increasing concentrations of NECA. Binding affinities were obtained through radioligand binding assays as detailed in Lagarias *et al.*, 2018.

	pIC ₅₀ /pEC ₅₀ ^a				K _i (μM) ^b			
	A ₃ R	A ₁ R	A _{2A} R	A _{2B} R	A ₃ R	A ₁ R	A _{2A} R	A _{2B} R
NECA only	8.94 ±0.1	9.00 ±0.1	8.80 ±0.1	8.18 ±0.1	ND	ND	ND	ND
K1	7.80 ±0.1****	9.07 ±0.2	7.75 ±0.1**	8.36 ±0.2	3.10	>100	2.67	ND
K10	7.15 ±0.1****	8.90 ±0.1	8.64 ±0.1	8.45 ±0.2	4.49	>60	>60	ND
K17	7.43 ±0.1****	8.80 ±0.2	8.48 ±0.1	8.40 ±0.2	4.16	>30	>60	ND
K18	6.61 ±0.1****	8.81 ±0.2	8.37 ±0.2	8.67 ±0.2	0.89	>100	>100	ND
K20	6.68 ±0.1****	7.38 ±0.1****	7.88 ±0.1**	8.14 ±0.2	0.91	1.09	7.29	ND
K23	7.35 ±0.1****	7.49 ±0.1****	7.94 ±0.1**	8.36 ±0.2	1.65	1.18	4.69	ND
K25	7.54 ±0.2****	9.01 ±0.2	8.68 ±0.1	8.38 ±0.1	1.55	>100	>100	ND
K32	7.54 ±0.2****	8.86 ±0.1	8.65 ±0.1	7.38 ±0.1*	2.4	>100	>100	ND

^aNegative logarithm of NECA concentration required to produce a half-maximal response in the absence (NECA only) or presence of 1 μM compound at each AR subtype

^bBinding affinity of potential antagonists as previously determined (Lagarias *et al.*, 2018)

Statistical significance compared to NECA only stimulation was determined by one-way ANOVA with Dunnett's post-test.

ND indicates not determined.

Statistical significance (*, $p < 0.05$; **, $p < 0.01$; ***, $p < 0.001$; ****, $p < 0.0001$) compared to NECA only stimulation was determined by one-way ANOVA with Dunnett's post-test.

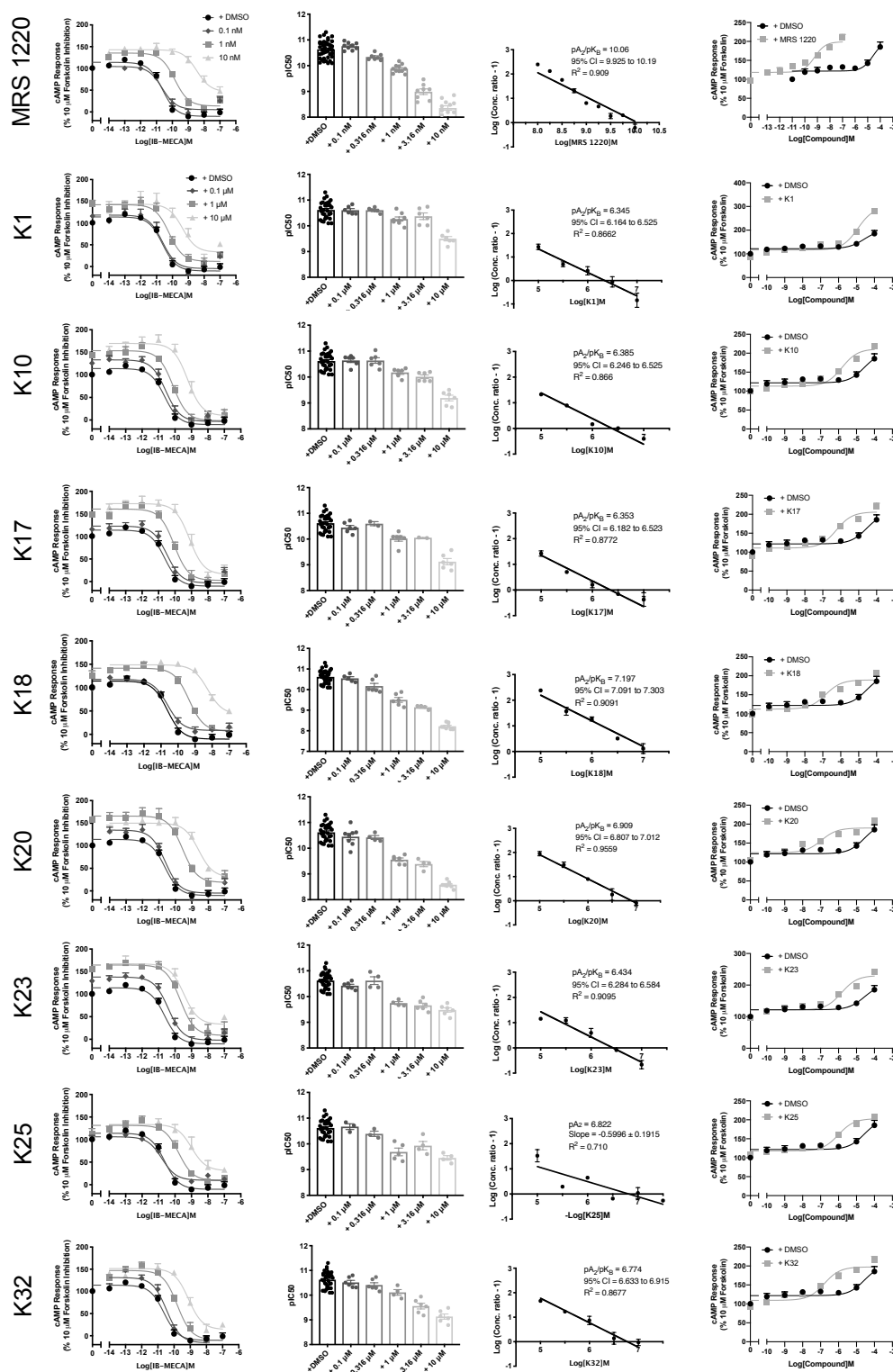


Figure 2. IB-MECA stimulated cAMP inhibition at WT A₃R: activity of MRS 1220 and potential antagonists. Flp-In-CHO cells (2000 cells/well) stably expressing WT A₃R were exposed to forskolin 10 μ M, IB-MECA and test compound/MRS 1220/DMSO control for 30 min and cAMP accumulation detected. **A)** Representative dose response curves are shown as mean \pm SEM expressed as percentage forskolin inhibition (10 μ M) relative to IB-MECA. Key indicated in K1 is identical for all 'K' test compounds shown. **B)** pIC₅₀ values for individual repeats including half-log concentration are shown as mean \pm SEM **C)** Schild analysis of data represented in **A/B**. A slope of 1 indicates a competitive antagonist. The x-axis is expressed as -log (molar concentration of antagonist) giving a negative Schild slope. **D)** Inverse agonism at the A₃R. cAMP accumulation following a 30-minute stimulation with forskolin (10 μ M) and increasing concentrations of antagonist/DMSO control was determined in WT A₃R expressing Flp-In-CHO cells. Representative dose response curves are shown as mean \pm SEM expressed as percentage forskolin (10 μ M), relative to IB-MECA.

Table 3. IB-MECA stimulated cAMP inhibition at WT A₃R: activity of MRS 1220 and potential antagonists. Forskolin stimulated cAMP inhibition was measured in Flp-In-CHO stably expressing A₃R following stimulation with 10 μM forskolin, compound at the indicated concentration and varying concentrations of IB-MECA.

		WT A ₃ R Flp-In-CHO					Inverse agonism
		pIC ₅₀ ^a	E _{min} ^b	Basal ^c	True Basal ^d	Span ^e	pEC ₅₀ ^f
IB-MECA only		10.64 ±0.1	-10.2 ±4.1	109.8 ±2.3	100.6 ±2.4	110.9 ±2.8	
MRS 1220	0.1 nM	10.61 ±0.1	5.3 ±4.3	104.4 ±4.6	106.3 ±3.3	99.2 ±6.0	9.21 ±0.2
	1 nM	9.85 ±0.1****	13.6 ±4.6*	135.4 ±3.7**	125.3 ±6.0***	121.8 ±5.7	
	10 nM	8.45 ±0.1****	46.4 ±7.3****	143.0 ±3.0***	135.2 ±3.8****	96.6 ±7.6	
K1	0.1 μM	10.52 ±0.1	-4.2 ±9.4	118.2 ±7.4	104.5 ±6.0	113.0 ±1.3	4.93 ±0.1
	1 μM	10.18 ±0.1*	21.9 ±7.0	141.9 ±10.1***	127.6 ±8.9*	117.5 ±6.4	
	10 μM	9.44 ±0.1****	36.3 ±7.9**	170.7 ±4.6****	161.0 ±6.8****	121.2 ±6.2	
K10	0.1 μM	10.60 ±0.1	-4.0 ±8.2	132.1 ±6.0**	125.9 ±6.2***	128.2 ±0.9	5.81 ±0.1
	1 μM	10.14 ±0.1	-2.0 ±7.6	152.9 ±6.2****	143.9 ±3.8****	137.5 ±4.8*	
	10 μM	9.20 ±0.1****	15.4 ±10.0	169.8 ±9.5****	156.2 ±7.0****	145.3 ±4.9***	
K17	0.1 μM	10.45 ±0.1	-5.4 ±8.7	121.1 ±9.3	120.4 ±6.2*	108.6 ±7.6	6.24 ±0.2
	1 μM	10.02 ±0.1**	2.5 ±6.6	160.7 ±7.3****	143.1 ±7.6****	138.3 ±5.8**	
	10 μM	9.12 ±0.1****	21.8 ±9.3*	173.4 ±8.1****	164.5 ±7.6****	147.5 ±6.6***	
K18	0.1 μM	10.61 ±0.1	8.4 ±4.0	117.7 ±3.7	107.5 ±4.9	109.3 ±5.2	6.84 ±0.2
	1 μM	9.43 ±0.1****	13.6 ±5.7	142.0 ±3.4****	130.7 ±5.0****	111.1 ±3.6	
	10 μM	8.25 ±0.1****	43.0 ±6.7****	148.8 ±2.3****	138.6 ±2.4****	118.5 ±6.2	
K20	0.1 μM	10.46 ±0.2	-8.4 ±9.9	124.3 ±2.1	113.6 ±4.1	115.4 ±9.8	6.96 ±0.2
	1 μM	9.52 ±0.1****	14.1 ±10.3*	168.3 ±3.1****	141.2 ±9.8****	118.1 ±8.7	
	10 μM	8.62 ±0.1****	35.0 ±9.6**	142.6 ±11.8***	130.4 ±12.5**	106.4 ±5.3	
K23	0.1 μM	10.42 ±0.1	-1.9 ±6.3	137.6 ±5.5****	130.3 ±7.7***	123.6 ±5.7	5.83 ±0.2
	1 μM	9.75 ±0.1****	8.7 ±8.6	165.9 ±2.5****	159.2 ±2.8****	125.6 ±1.2	
	10 μM	9.48 ±0.1****	33.0 ±6.5***	167.9 ±7.1****	167.9 ±7.9****	135.1 ±8.5**	
K25	0.1 μM	10.67 ±0.1	9.9 ±4.2	106.8 ±6.8	99.1 ±6.7	107.1 ±4.7	6.01 ±0.1
	1 μM	9.69 ±0.1****	9.0 ±5.9	125.8 ±2.3*	120.0 ±7.5	118.0 ±3.8	

K32	10 μ M	9.46 \pm 0.1****	31.1 \pm 9.0**	135.1 \pm 5.2***	121.7 \pm 6.3*	108.0 \pm 3.8	
	0.1 μ M	10.54 \pm 0.1	19.3 \pm 7.2	121.7 \pm 5.9	94.8 \pm 3.0	141.0 \pm 8.9***	6.79 \pm 0.2
	1 μ M	9.70 \pm 0.2****	-17.8 \pm 6.5	140.0 \pm 3.9****	117.4 \pm 3.5	157.8 \pm 7.2****	
	10 μ M	9.04 \pm 0.1****	17.9 \pm 8.5	145.6 \pm 5.1****	128.8 \pm 7.7*	127.7 \pm 9.5	

^aNegative logarithm of IB-MECA concentration required to produce a half-maximal response in the absence (IB-MECA only) or presence of 0.1, 1 or 10 μ M compound

^bMinimum cAMP accumulation of IB-MECA as % 10 μ M forskolin response relative to IB-MECA only; the lower plateau of the fitted sigmoidal dose response curve

^cThe upper plateau of the fitted sigmoidal dose response curve corresponding to % 10 μ M forskolin inhibition, relative to IB-MECA

^dThe cAMP accumulation when stimulated with compound at the indicated concentration and 10 μ M forskolin stimulation only

^eThe difference between E_{min} and basal signaling

^fValue reported to determine inverse agonism: Negative logarithm of compound concentration required to produce a half-maximal response

Statistical significance (*, $p < 0.05$; **, $p < 0.01$; ***, $p < 0.001$; ****, $p < 0.0001$) compared to 'IB-MECA only' was determined by one-way ANOVA with Dunnett's post-test.

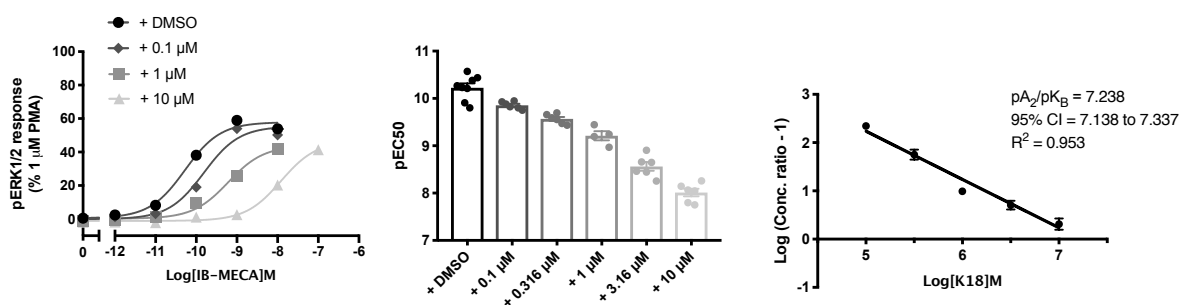


Figure 3. K18 also reduced levels of agonist stimulated ERK1/2 phosphorylation. pERK1/2 was detected in Flp-In-CHO cells stably expressing A₃R (2000 cells/well) stimulated for 5 minutes with IB-MECA, with or without K18. **A)** Representative dose response curves for IB-MECA with K18 at the indicated concentration or DMSO control shown as mean \pm SEM expressed as % 1 μ M PMA response. **B)** pEC₅₀ values for individual repeats are shown as mean \pm SEM. **C)** Schild analysis of data represented in **A/B**.

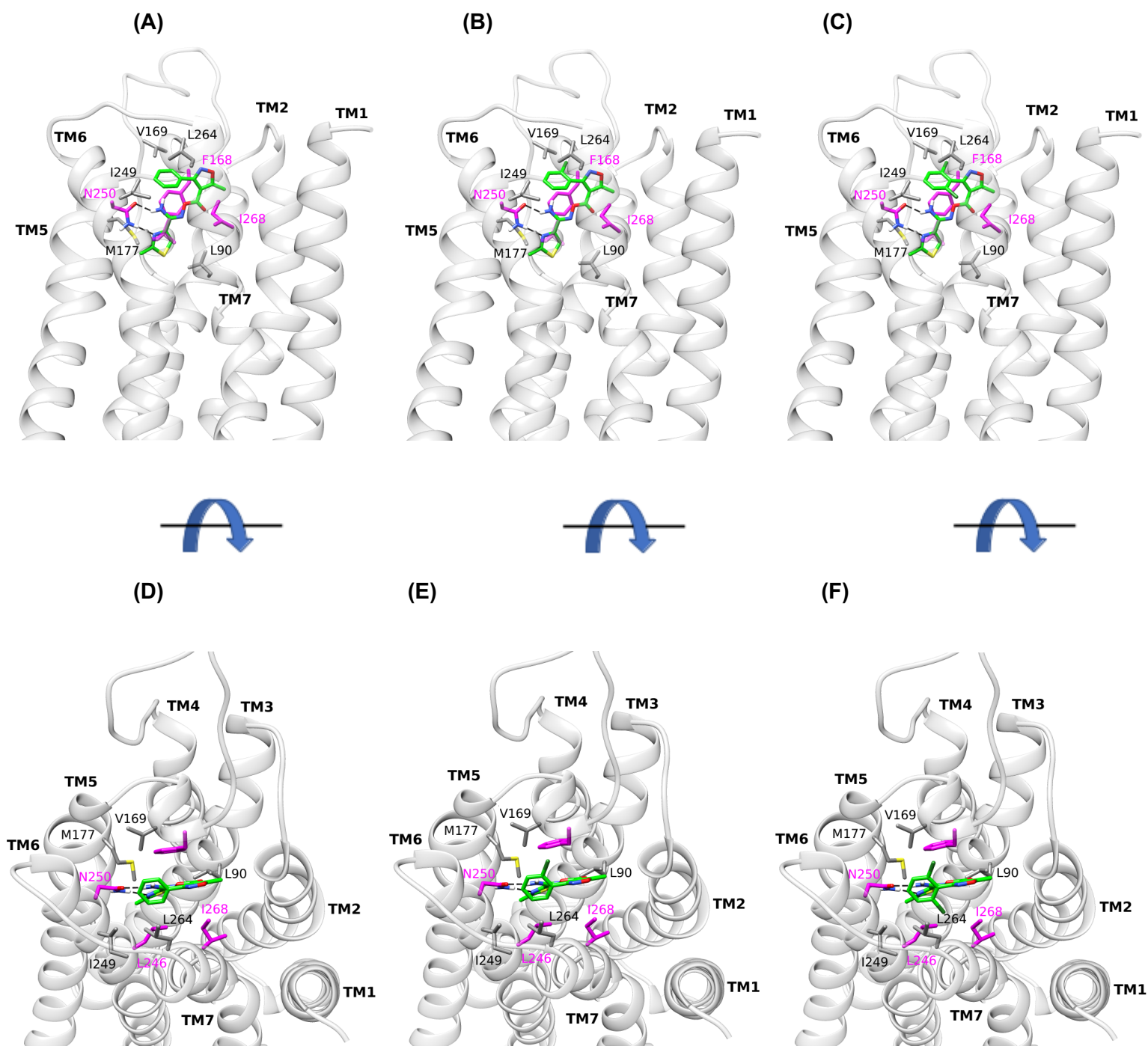


Figure 4. Orthosteric binding area average structure of WT A₃R in complex with K5, K17 and K18 from MD simulations with Amber14ff. Side (A), top (D) view of K5 complex; side (B), top (E) view of K17 complex; side (C), top (F) view of K18 complex. Side chains of critical residues for binding indicated from the MD simulations are shown in sticks. Residues L90^{3,32}, V169^{5,30}, M177^{5,40}, I249^{6,54} and L264^{7,34}, in which carbon atoms are shown in grey, were confirmed experimentally; in residues F168^{5,29}, L246^{6,51}, I268^{7,39} and N250^{6,55} carbon atoms are shown in magenta; nitrogen, oxygen and sulfur atoms are shown in blue, red and yellow respectively.

Table 4. Effective binding energies (ΔG_{eff}) and energy components (E_{vdW} , E_{EL} , ΔG_{solv}) in kcal mol⁻¹ calculated using the MM-PBSA method for binding of K5, K17 and K18 to the A₃R orthosteric binding area.

	E_{vdW}^a	E_{EL}^b	ΔG_{solv}^c	ΔG_{eff}^d	pK_B/pK_i^e		
					Schild analysis ^f	NanoBRET ^g	Radioligand binding ^h
MRS 1220					10.07	9.99 ± 0.04	8.2 – 9.2
K5	-42.0 ± 2.7	-9.6 ± 5.2	30.8 ± 4.3	-20.8 ± 4.3	ND	6.06 ± 0.09	5.02
K17	-47.0 ± 2.4	-8.8 ± 2.7	29.8 ± 2.9	-25.9 ± 3.6	6.35	6.33 ± 0.03	5.38
K18	-46.3 ± 2.9	-7.5 ± 2.4	26.9 ± 3.1	-26.9 ± 2.7	7.20	6.92 ± 0.10	6.05

^avdW energy of binding calculated using molecular mechanics

^bElectrostatic energy of binding calculated using molecular mechanics

^cDifference in solvation energy between the complex, the protein and the ligand, i.e. $G_{\text{complex, solv}} - (G_{\text{protein, solv}} + G_{\text{ligand, solv}})$

^dEffective binding free energy calculated as $\Delta G_{\text{eff}} = \Delta E_{\text{MM}} + \Delta G_{\text{solv}}$; in Table 4, $\Delta E_{\text{MM}} = E_{\text{vdW}} + E_{\text{EL}}$ (see Materials and Methods)

^eEquilibrium dissociation constant of MRS 1220, K5, K17 and K18 as determined through three independent experimental approaches: Schild analysis (pK_B), NanoBRET (pK_i) or radioligand binding (pK_i)

^f pK_B obtained through Schild analysis in A₃R stably expressing Flp-In CHO cells

^g pK_i (mean ± SEM) obtained in NanoBRET binding assays using Nluc-A₃R stably expressing HEK 293 cells and determined through fitting our “Kinetics of competitive binding, rapid competitor dissociation” model or in the case of MRS 1220 through fitting with the ‘Kinetics of competitive binding’ model with a determined K_{on} (k_3) and K_{off} (k_4) rate of $3.25 \pm 0.28 \times 10^8 \text{ M}^{-1} \text{ min}^{-1}$ and $0.0248 \pm 0.005 \text{ min}^{-1}$, respectively

^h pK_i values previously published for K5, K17 and K18 (Lagarias *et al.*, 2018) or MRS 1220 (Stoddart *et al.*, 2015) through radioligand binding assays.

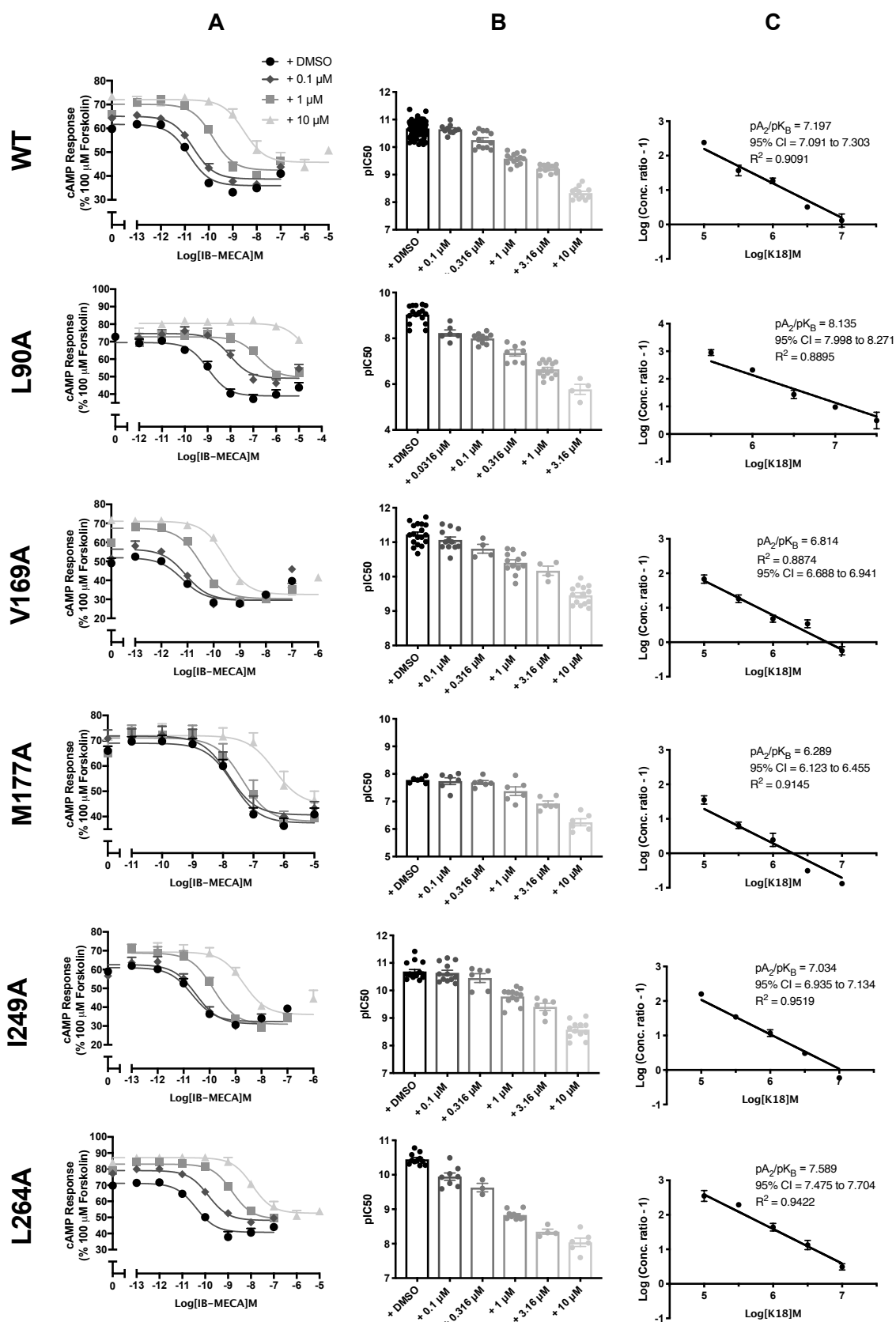


Figure 5. IB-MECA stimulated cAMP inhibition at WT or mutant A₃R with increasing concentrations of K18. Flp-In-CHO cells (2000 cells/well) stably expressing WT or mutant A₃R were exposed to forskolin 10 μM, IB-MECA and K18 at varying concentrations for 30 min and cAMP accumulation detected. **A)** Representative dose response curves are shown as mean ± SEM expressed as percentage maximum forskolin response (100 μM). **B)** pIC₅₀ values for individual repeats including half-log concentration are shown as mean ± SEM **C)** Schild analysis of data represented in **A/B**.

Table 5. Antagonistic potency of K18 at A₃R mutants. cAMP accumulation as measured in Flp-In-CHO cells stably expressing WT or mutant A₃R following stimulation with 10 μM forskolin, varying concentrations of IB-MECA and +/-K18 at the indicated concentration.

+ DMSO					
	pIC₅₀^a	E_{min}^b	Basal^c	True Basal^d	Span^e
WT	10.64 ±0.1	33.5± 2.0	64.7 ±1.8	58.7 ±0.5	31.2 ±2.6
L90A	8.67 ±0.1****	36.8 ±1.8	69.5 ±1.7	67.8 ±1.5****	32.8 ±2.4
V169A	11.23 ±0.1****	29.5 ±1.6	57.0 ±1.4**	53.8 ±1.5**	27.5 ±2.0
M177A	7.64 ±0.1****	38.0 ±2.2	70.1 ±1.5	66.7 ±1.3****	32.1 ±2.6
I249A	10.67 ±0.1	32.9 ±1.9	61.0 ±1.6	61.2 ±1.0	32.4 ±1.6
L264A	10.29 ±0.1*	38.4 ±1.7	64.8 ±1.6	68.8 ±1.3****	26.5 ±2.2
V169E	11.48 ±0.1****	38.1 ± 1.5	66.1 ±2.1	67.4 ±1.6***	28.1 ±2.4
+ 0.1 μM K18					
WT	10.65 ±0.1	38.7 ±0.9	65.1 ±0.9	64.2 ±0.9	26.4 ±1.2
L90A	8.00 ±0.2****	49.1 ±1.6***	74.6 ±1.4****	72.0 ±2.6	25.5 ±2.1
V169A	11.07 ±0.1 **	29.6 ±1.3***	56.4 ±1.2***	54.1 ±2.3**	26.8 ±1.7
M177A	7.81 ±0.2****	40.6 ±2.7	71.9 ±1.9**	70.9 ±3.4	31.2 ±3.3
I249A	10.52 ±0.1	31.1 ±1.8**	62.6 ±1.3	65.5 ±1.4	31.5 ±2.1
L264A	9.87 ±0.1****	48.2 ±1.2***	79.1 ±0.9****	77.3 ±2.2***	31.0 ±1.5
V169E	11.21 ±0.1****	39.7 ± 1.0	74.7 ±1.3****	73.7 ±1.6*	35.0 ±1.6*
+ 1 μM K18					
WT	9.50 ±0.1	42.4 ±1.1	70.1 ±0.9	64.4 ±1.5	27.7 ±1.4
L90A	6.80 ±0.2****	49.6 ±2.6*	72.7 ±1.4	69.5 ±3.0	23.2 ±2.8
V169A	10.49 ±0.1****	30.4 ±1.1****	67.4 ±1.0	65.4 ±1.3	37.1 ±1.3*
M177A	7.36 ±0.2****	38.1 ±3.0	71.1 ±1.9	65.1 ±2.9	33.0 ±3.4
I249A	9.86 ±0.1*	30.9 ±1.7***	68.8 ±1.4	71.9 ±2.4	37.9 ±2.1**
L264A	8.83 ±0.1****	49.1 ±1.7	83.1 ±0.9****	79.3 ±2.0****	34.0 ±1.9
V169E	10.49 ±0.1****	43.4 ± 1.0	81.1 ±0.9****	78.8 ±1.2****	37.7 ±1.4**
+ 10 μM K18					
WT	8.33 ±0.2	45.8 ±1.6	72.1 ±1.1	68.8 ±1.5	26.3 ±1.8
L90A	5.58 ±0.4****	55.4 ±6.8	80.4 ±1.3***	73.6 ±2.1	25.0 ±6.7
V169A	9.55 ±0.1 ****	32.6 ±1.0*	71.1 ±0.7	68.6 ±0.7	38.6 ±1.1*
M177A	6.31 ±0.3****	44.7 ±4.0	72.0 ±1.5	67.7 ±2.5	27.4 ±4.1
I249A	8.69 ±0.2*	36.1 ±2.3	69.3 ±2.5	72.9 ±1.2	33.2 ±2.5
L264A	7.94 ±0.1	52.6 ±1.7	87.1 ±1.1****	81.5 ±2.6***	34.5 ±1.9
V169E	9.23 ±0.1***	43.9 ± 1.1	83.1 ±0.8****	80.4 ±1.6**	39.2 ±1.3*

^aNegative logarithm of IB-MECA concentration required to produce a half-maximal response

^bMinimum cAMP accumulation of IB-MECA as %100 μM forskolin. The lower plateau of the fitted sigmoidal dose response curve

^cThe upper plateau of the fitted sigmoidal dose response curve corresponding %100 μM forskolin

^dThe cAMP accumulation when stimulated with 10 μM forskolin only + DMSO/K18 at the indicated concentration

^eThe difference between E_{min} and basal signalling

Statistical significance (*, $p < 0.05$; **, $p < 0.01$; ***, $p < 0.001$; ****, $p < 0.0001$) compared to WT IB-MECA stimulation +/- K18 at each indicated concentration was determined by one-way ANOVA with Dunnett's post-test.

References

- Alexander, S.P., Kelly, E., Marrion, N.V., Peters, J.A., Faccenda, E., Harding, S.D., et al. (2017). THE CONCISE GUIDE TO PHARMACOLOGY 2017/18: Overview. *British Journal of Pharmacology* 174 Suppl 1: S1–S16.
- Arruda, M.A., Stoddart, L.A., Gherbi, K., Briddon, S.J., Kellam, B., and Hill, S.J. (2017). A Non-imaging High Throughput Approach to Chemical Library Screening at the Unmodified Adenosine-A3 Receptor in Living Cells. *Front Pharmacol* 8: 908.
- Bayly, C.I., Cieplak, P., Cornell, W.D., and Kollman, P.A. (1993). A Well-Behaved Electrostatic Potential Based Method Using Charge Restraints for Deriving Atomic Charges - the Resp Model. *Journal of Physical Chemistry* 97: 10269–10280.
- Berendsen, H.J.C., Postma, J.P.M., van Gunsteren, W.F., DiNola, A., and Haak, J.R. (1984). Molecular dynamics with coupling to an external bath. *Journal of Chemical Physics* 81: 3684.
- Carlsson, J., Yoo, L., Gao, Z.-G., Irwin, J.J., Shoichet, B.K., and Jacobson, K.A. (2010). Structure-based discovery of A2A adenosine receptor ligands. *J. Med. Chem.* 53: 3748–3755.
- Carpenter, B., Nehmé, R., Warne, T., Leslie, A.G.W., and Tate, C.G. (2016). Structure of the adenosine A(2A) receptor bound to an engineered G protein. *Nature* 536: 104–107.
- Case, D.A., Babin, V., Berryman, J.T., Betz, R.M., Cai, Q., Cerutti, D.S., et al. (2014). AMBER 14 (University of California, San Francisco).
- Chen, J.-F., Eltzschig, H.K., and Fredholm, B.B. (2013). Adenosine receptors as drug targets - what are the challenges? *Nat Rev Drug Discov* 12: 265–286.
- Cheng, R.K.Y., Segala, E., Robertson, N., Deflorian, F., Dore, A.S., Errey, J.C., et al. (2017). Structures of Human A1 and A2A Adenosine Receptors with Xanthines Reveal Determinants of Selectivity. *Structure* 25: 1275–1285.e4.
- Cheng, Y., and Prusoff, W.H. (1973). Relationship between the inhibition constant (K_1) and the concentration of inhibitor which causes 50 per cent inhibition (I_{50}) of an enzymatic reaction. *Biochem. Pharmacol.* 22: 3099–3108.
- Curtis, M.J., Alexander, S., Cirino, G., Docherty, J.R., George, C.H., Giembycz, M.A., et al. (2018). Experimental design and analysis and their reporting II: updated and simplified guidance for authors and peer reviewers. *British Journal of Pharmacology* 175: 987–993.
- Darden, T., York, D., and Pedersen, L. (1993). Particle mesh Ewald: An $N \cdot \log(N)$ method for Ewald sums in large systems. *Journal of Chemical Physics* 98: 10089.
- Dickson, C.J., Madej, B.D., Skjevik, A.A., Betz, R.M., Teigen, K., Gould, I.R., et al. (2014). Lipid14: The Amber Lipid Force Field. *J Chem Theory Comput* 10: 865–879.
- Dore, A.S., Robertson, N., Errey, J.C., Ng, I., Hollenstein, K., Tehan, B., et al. (2011). Structure of the adenosine A(2A) receptor in complex with ZM241385 and the xanthines XAC and caffeine. *Structure* 19: 1283–1293.

Draper-Joyce, C.J., Khoshouei, M., Thal, D.M., Liang, Y.-L., Nguyen, A.T.N., Furness, S.G.B., et al. (2018). Structure of the adenosine-bound human adenosine A1 receptor-Gi complex. *Nature* 558: 559–563.

Eldridge, M.D., Murray, C.W., Auton, T.R., Paolini, G.V., and Mee, R.P. (1997). Empirical scoring functions: I. The development of a fast empirical scoring function to estimate the binding affinity of ligands in receptor complexes. *J. Comput. Aided Mol. Des.* 11: 425–445.

Essmann, U., Lalith Perera, Berkowitz, M.L., Darden, T., Lee, H., and Pedersen, L.G. (1995). A smooth particle mesh Ewald method. *Journal of Chemical Physics* 103: 8577.

Floris, M., Sabbadin, D., Medda, R., Bulfone, A., and Moro, S. (2012). Adenosiland: walking through adenosine receptors landscape. *Eur J Med Chem* 58: 248–257.

Fredholm, B.B., Ijzerman, A.P., Jacobson, K.A., Linden, J., and Mueller, C.E. (2011). International Union of Basic and Clinical Pharmacology. LXXXI. Nomenclature and Classification of Adenosine Receptors-An Update. *Pharmacol. Rev.* 63: 1–34.

Frisch, M.J., Trucks, G.W., Schlegel, H.B., Scuseria, G.E., Rob, M.A., and Pople, J.A. (2003). *Gaussian 03* (Wallingford, CT).

Gao, Z.-G., Chen, A., Barak, D., Kim, S.-K., Müller, C.E., and Jacobson, K.A. (2002). Identification by site-directed mutagenesis of residues involved in ligand recognition and activation of the human A3 adenosine receptor. *J. Biol. Chem.* 277: 19056–19063.

Gessi, S., Merighi, S., Varani, K., Leung, E., Mac Lennan, S., and Borea, P.A. (2008). The A3 adenosine receptor: an enigmatic player in cell biology. *Pharmacol. Ther.* 117: 123–140.

Giraldo, J., Serra, J., Roche, D., and Rovira, X. (2007). Assessing receptor affinity for inverse agonists: Schild and Cheng-Prusoff methods revisited. *Curr Drug Targets* 8: 197–202.

Glukhova, A., Thal, D.M., Nguyen, A.T., Vecchio, E.A., Jörg, M., Scammells, P.J., et al. (2017). Structure of the Adenosine A1 Receptor Reveals the Basis for Subtype Selectivity. *Cell* 168: 867–877.e13.

Graham, S., Combes, P., Crumiere, M., Klotz, K.N., and Dickenson, J.M. (2001). Regulation of p42/p44 mitogen-activated protein kinase by the human adenosine A(3) receptor in transfected CHO cells. *Eur. J. Pharmacol.* 420: 19–26.

Haeusler, D., Grassinger, L., Fuchshuber, F., Hoerleinsberger, W.J., Hoftberger, R., Leisser, I., et al. (2015). Hide and seek: a comparative autoradiographic in vitro investigation of the adenosine A3 receptor. *Eur. J. Nucl. Med. Mol. Imaging* 42: 928–939.

Harding, S.D., Sharman, J.L., Faccenda, E., Southan, C., Pawson, A.J., Ireland, S., et al. (2018). The IUPHAR/BPS Guide to PHARMACOLOGY in 2018: updates and expansion to encompass the new guide to IMMUNOPHARMACOLOGY. *Nucleic Acids Res.* 46: D1091–D1106.

Homeyer, N., and Gohlke, H. (2013). FEW: A workflow tool for free energy calculations of ligand binding. *J Comput Chem* 34: 965–973.

Humphrey, W., Dalke, A., and Schulten, K. (1996). VMD: Visual molecular dynamics. *Journal of Molecular Graphics & Modelling* 14: 33–38.

Jaakola, V.-P., Griffith, M.T., Hanson, M.A., Cherezov, V., Chien, E.Y.T., Lane, J.R., et al. (2008). The 2.6 angstrom crystal structure of a human A2A adenosine receptor bound to an antagonist. *Science* 322: 1211–1217.

Jones, G., Willett, P., Glen, R.C., Leach, A.R., and Taylor, R. (1997). Development and validation of a genetic algorithm for flexible docking. *J. Mol. Biol.* 267: 727–748.

Jorgensen, W.L., Chandrasekhar, J., Madura, J.D., Impey, R.W., and Klein, M.L. (1983). Comparison of Simple Potential Functions for Simulating Liquid Water. *Journal of Chemical Physics* 79: 926–935.

Katritch, V., Jaakola, V.-P., Lane, J.R., Lin, J., Ijzerman, A.P., Yeager, M., et al. (2010). Structure-Based Discovery of Novel Chemotypes for Adenosine A(2A) Receptor Antagonists. *J. Med. Chem.* 53: 1799–1809.

Klotz, K.N., Hessling, J., Hegler, J., Owman, C., Kull, B., Fredholm, B.B., et al. (1998). Comparative pharmacology of human adenosine receptor subtypes - characterization of stably transfected receptors in CHO cells. *Naunyn Schmiedebergs Arch. Pharmacol.* 357: 1–9.

Knight, A., Hemmings, J.L., Winfield, I., Leuenberger, M., Frattini, E., Frenguelli, B.G., et al. (2016). Discovery of Novel Adenosine Receptor Agonists That Exhibit Subtype Selectivity. *J. Med. Chem.* 59: 947–964.

Kolb, P., Phan, K., Gao, Z.-G., Marko, A.C., Sali, A., and Jacobson, K.A. (2012). Limits of Ligand Selectivity from Docking to Models: In Silico Screening for A(1) Adenosine Receptor Antagonists. *PLoS ONE* 7(11): e49910

Koynova, R., and Caffrey, M. (1998a). Phases and phase transitions of the phosphatidylcholines. *Biochim. Biophys. Acta* 1376: 91–145.

Lagarias, P., Vrontaki, E., Lambrinidis, G., Stamatis, D., Convertino, M., Ortore, G., et al. (2018). Discovery of Novel Adenosine Receptor Antagonists through a Combined Structure- and Ligand-Based Approach Followed by Molecular Dynamics Investigation of Ligand Binding Mode. *J Chem Inf Model* 58: 794–815.

Lebon, G., Edwards, P.C., Leslie, A.G.W., and Tate, C.G. (2015). Molecular Determinants of CGS21680 Binding to the Human Adenosine A2A Receptor. *Mol. Pharmacol.* 87: 907–915.

Lebon, G., Warne, T., Edwards, P.C., Bennett, K., Langmead, C.J., Leslie, A.G.W., et al. (2011). Agonist-bound adenosine A2A receptor structures reveal common features of GPCR activation. *Nature* 474: 521–525.

Lenselink, E.B., Beuming, T., van Veen, C., Massink, A., Sherman, W., van Vlijmen, H.W.T., et al. (2016). In search of novel ligands using a structure-based approach: a case study on the adenosine A2A receptor. *J. Comput. Aided Mol. Des.* 30: 863–874.

Liu, W., Chun, E., Thompson, A.A., Chubukov, P., Xu, F., Katritch, V., et al. (2012). Structural basis for allosteric regulation of GPCRs by sodium ions. *Science* 337: 232–236.

Maier, J.A., Martinez, C., Kasavajhala, K., Wickstrom, L., Hauser, K.E., and Simmerling, C. (2015). ff14SB: Improving the Accuracy of Protein Side Chain and Backbone Parameters from ff99SB. *J Chem Theory Comput* 11: 3696–3713.

Massova, I., and Kollman, P.A. (2000). Combined molecular mechanical and continuum solvent approach (MM-PBSA/GBSA) to predict ligand binding. *Perspectives in Drug Discovery and Design* 18: 113–135.

May, L.T., Bridge, L.J., Stoddart, L.A., Briddon, S.J., and Hill, S.J. (2011). Allosteric interactions across native adenosine-A3 receptor homodimers: quantification using single-cell ligand-binding kinetics. *Faseb J.* 25: 3465–3476.

Meng, X.-Y., Zhang, H.-X., Mezei, M., and Cui, M. (2011). Molecular Docking: A Powerful Approach for Structure-Based Drug Discovery. *Curr Comput Aided Drug Des* 7: 146–157.

Miller, B.R.I., McGee, T.D.J., Swails, J.M., Homeyer, N., Gohlke, H., and Roitberg, A.E. (2012). MMPBSA.py: An Efficient Program for End-State Free Energy Calculations. *J Chem Theory Comput* 8: 3314–3321.

Miwatashi, S., Arikawa, Y., Matsumoto, T., Uga, K., Kanzaki, N., Imai, Y.N., et al. (2008). Synthesis and biological activities of 4-phenyl-5-pyridyl-1,3-thiazole derivatives as selective adenosine A3 antagonists. *Chem. Pharm. Bull.* 56: 1126–1137.

Motulsky, H.J. Interpreting the extra sum-of squares F test. https://www.graphpad.com/guides/prism/7/curve-fitting/index.htm?reg_interpreting_comparison_of_mod_2.htm

Motulsky, H.J., and Mahan, L.C. (1984). The Kinetics of Competitive Radioligand Binding Predicted by the Law of Mass-Action. *Mol. Pharmacol.* 25: 1–9.

Okamura, T., Kurogi, Y., Hashimoto, K., Sato, S., Nishikawa, H., Kiryu, K., et al. (2004). Structure-activity relationships of adenosine A3 receptor ligands: new potential therapy for the treatment of glaucoma. *Bioorg. Med. Chem. Lett.* 14: 3775–3779.

Pettersen, E.F., Goddard, T.D., Huang, C.C., Couch, G.S., Greenblatt, D.M., Meng, E.C., et al. (2004). UCSF chimera - A visualization system for exploratory research and analysis. *J Comput Chem* 25: 1605–1612.

Ryckaert, J.-P., Ciccotti, G., and Berendsen, H.J.C. (1977). Numerical integration of the Cartesian Equations of Motion of a System with Constraints: Molecular Dynamics of n-Alkanes. *Journal of Computational Physics* 23: 327–341.

Schild, H.O. (1947). pA, a new scale for the measurement of drug antagonism. *Br J Pharmacol Chemother* 2: 189–206.

Schulte, G., and Fredholm, B.B. (2002). Signaling pathway from the human adenosine A(3) receptor expressed in Chinese hamster ovary cells to the extracellular signal-regulated kinase 1/2. *Mol. Pharmacol.* 62: 1137–1146.

Sexton, P.M., and Christopoulos, A. (2018). To Bind or Not to Bind: Unravelling GPCR Polypharmacology. *Cell* 172: 636–638.

Stamatis, D, Lagarias, P, Barkan, K, Vrontaki, E, Ladds G and Antonios Kolocouris. Structural Characterization of Agonist Binding to A3 Adenosine Receptor through Biomolecular Simulations and Mutagenesis Experiments. Submitted to *J. Med. Chem*

Stoddart, L.A., Johnstone, E.K.M., Wheal, A.J., Goulding, J., Robers, M.B., Machleidt, T., et al. (2015). Application of BRET to monitor ligand binding to GPCRs. *Nat. Methods* 12: 661–663.

Stoddart, L.A., Kilpatrick, L.E., and Hill, S.J. (2018). NanoBRET Approaches to Study Ligand Binding to GPCRs and RTKs. *Trends Pharmacol. Sci.* 39: 136–147.

Stoddart, L.A., Vernall, A.J., Denman, J.L., Briddon, S.J., Kellam, B., and Hill, S.J. (2012). Fragment screening at adenosine-A(3) receptors in living cells using a fluorescence-based binding assay. *Chem. Biol.* 19: 1105–1115.

Sykes, D.A., Stoddart, L.A., Kilpatrick, L.E., and Hill, S.J. (2019). Binding kinetics of ligands acting at GPCRs. *Mol. Cell. Endocrinol.* 485: 9–19.

Tunçer, S., Gurbanov, R., Sheraj, I., Solel, E., Esenturk, O., and Banerjee, S. (2018). Low dose dimethyl sulfoxide driven gross molecular changes have the potential to interfere with various cellular processes. *Sci Rep* 8: 14828.

Verdonk, M.L., Chessari, G., Cole, J.C., Hartshorn, M.J., Murray, C.W., Nissink, J.W.M., et al. (2005). Modeling water molecules in protein-ligand docking using GOLD. *J. Med. Chem.* 48: 6504–6515.

Wang, J.M., Wolf, R.M., Caldwell, J.W., Kollman, P.A., and Case, D.A. (2004). Development and testing of a general amber force field. *J Comput Chem* 25: 1157–1174.

Xu, F., Wu, H., Katritch, V., Han, G.W., Jacobson, K.A., Gao, Z.-G., et al. (2011). Structure of an agonist-bound human A2A adenosine receptor. *Science* 332: 322–327.

Zhang, G., Liu, Y., Ruoho, A.E., and Hurley, J.H. (1997). Structure of the adenylyl cyclase catalytic core. *Nature* 386: 247–253.

Regression with Prism 8: 'Ambiguous'. https://www.graphpad.com/guides/prism/8/curve-fitting/reg_analysischeck_nonlin_ambiguous.htm